In vivo functional genomics identifies essentiality of potassium homeostasis in medulloblastoma

Jerry J. Fan[1,2,3,*], Xin Wang[1,2,*], Anders W. Erickson[1,2,*], Patryk Skowron[1,2,*], Xian Wang[1,2,4], Xin Chen[1,2], Guanqiao Shan[4], Shahrzad Bahrampour[1,2], Yi Xiong[1,2,5,6], Weifan Dong[1,2,3], Namal Abeysundara[1,2], Michelle A. Francisco[1,2], Ronwell J. Pusong[1,2], Raúl A. Suárez[1,2], Hamza Farooq[1,2,7], Borja L. Holgado[1,2], Xiaochong Wu[1,2], Craig Daniels[1,2], Adam J. Dupuy[8], Juan Cadiñanos[9], Allan Bradley[10], Anindya Bagchi[11], Branden S. Moriarity[12], David A. Largaespada[12], A. Sorana Morrissy[1,2], Vijay Ramaswamy[1,2,13], Stephen C. Mack[1,2], Livia Garzia[1,2], Peter B. Dirks[1,2,3,7,14], Siyi Wanggou[1,2,5,6], Xuejun Li[5,6], Yu Sun[4], Michael D. Taylor[1,2,7,14,#], Xi Huang[1,2,3,#]

[1] Developmental & Stem Cell Biology Program, The Hospital for Sick Children, Toronto, Ontario, M5G 0A4, Canada

[2] Arthur and Sonia Labatt Brain Tumour Research Centre, The Hospital for Sick Children, Toronto, Ontario, M5G 0A4, Canada

[3] Department of Molecular Genetics, University of Toronto, Toronto, Ontario, M5S 1A8, Canada

[4] Department of Mechanical and Industrial Engineering, University of Toronto, Toronto, Ontario, M5S 3E1, Canada

[5] Department of Neurosurgery, Xiangya Hospital, Central South University, Changsha, Hunan, 410008, China

[6] Hunan International Scientific and Technological Cooperation Base of Brain Tumor Research, Xiangya Hospital, Central South University, Changsha, Hunan, 410008, China

[7] Department of Laboratory Medicine and Pathobiology, University of Toronto, Toronto, Ontario, M5S 3E1, Canada

[8] Department of Anatomy & Cell Biology, Carver College of Medicine, University of Iowa, Iowa City, Iowa, 52246, USA

[9] Instituto de Medicina Oncológica y Molecular de Asturias (IMOMA), Oviedo, 33193, Spain

[10] The Wellcome Trust Sanger Institute, Genome Campus, Hinxton, Cambridge, CB10 1SA, UK

[11] Tumor Initiation and Maintenance Program, Sanford Burnham Prebys Medical Discovery Institute, La Jolla, CA, 92037, USA

[12] Masonic Cancer Center, Department of Pediatrics, and Center for Genome Engineering, University of Minnesota, Minneapolis, MN, 55455, USA

[13] Department of Paediatrics, University of Toronto, Toronto, Ontario, M5G 1X8, Canada

[14] Department of Surgery, University of Toronto, Toronto, Ontario, M5S 1A8, Canada

* Co-first authors

[#] Correspondence:

Xi Huang: xi.huang@sickkids.ca

Michael D. Taylor: mdt.cns@gmail.com

ABSTRACT

Distinguishing tumor maintenance genes from initiation, progression, and passenger genes is fundamental for developing effective cancer therapy. We engineered a Lazy Piggy screening system to first dysregulate and later restore gene expression using the Sleeping Beauty/piggyBac hybrid transposon. *In vivo* Lazy Piggy insertion and remobilization deplete insertions non-essential for tumor survival while enriching for maintenance insertions, uncovering potassium channels in the maintenance of medulloblastoma, the most common pediatric brain malignancy. KCNB2 is the most overexpressed potassium channel in human medulloblastoma, and Kcnb2 knockout in mice diminishes the replicative potential of medulloblastoma-propagating cells to mitigate tumor growth. Mechanistically, Kcnb2 governs potassium homeostasis to regulate plasma membrane tension-gated EGFR signaling, which drives the proliferative expansion of medulloblastoma-propagating cells. Collectively, our Lazy Piggy functional genomics reveals potassium homeostasis as a tumor maintenance essentiality and elucidates a mechanism by which potassium homeostasis integrates biomechanical and biochemical signaling to promote medulloblastoma aggression.

INTRODUCTION

The ability to distinguish cancer maintenance drivers, which are required to sustain tumor growth, from ineffective targets (initiation, progression, and passenger events) is critical for the development of cancer therapeutics. Continued mutagenesis during clonal expansion yields new subclones with distinct mutational landscapes that contribute to tumor progression and maintenance. Initiation drivers confer tumor-forming capacity to normal cells but may no longer be required after tumor formation. Progression drivers enhance future malignancy but are not essential for tumor maintenance at present. Maintenance drivers sustain tumor survival and growth, and among these, only targeting maintenance drivers causes clonal collapse and tumor regression. Insertional mutagenesis systems, such as Sleeping Beauty (SB) and piggyBac (PB), are used to identify cancer drivers by “cutting-and-pasting” a DNA transposon randomly across the genome, causing gain- or loss-of-function mutations at target sites (Beckmann et al., 2019; Dupuy et al., 2005; Genovesi et al., 2013; Kas et al., 2017; Keng et al., 2009; Moriarity et al., 2015; Morrissy et al., 2016; Rahrmann et al., 2013; Starr et al., 2009, 2011; Wu et al., 2012). While insertional mutagenesis screens discern driver from passenger events, they cannot categorize cancer drivers (initiation, progression, or maintenance). To address this, we developed a novel functional genomics approach to uncover cancer maintenance drivers in medulloblastoma (MB).

MB is the most common pediatric malignant brain tumor (Ostrom et al., 2021). Standard-of-care consists of surgical resection, chemotherapy, and craniospinal irradiation. Although current treatments have achieved long-term survival in ~70% of patients, this survival rate has stagnated over the last 30 years despite deeper understanding of MB genomics (Johnston et al., 2015). Furthermore, long-term sequelae due to both disease and therapy impairs quality of life of MB survivors (Mulhern et al., 2004). Together, this highlights the need to develop novel therapeutic targets with minimal toxicity to the developing central nervous system. MB is comprised of four molecularly distinct subgroups: WNT, Sonic Hedgehog (SHH), Group 3, and Group 4 (Taylor

et al., 2012). SHH MB encompasses 30% of all cases. Genetically engineered mouse models (Goodrich et al., 1997; Mao et al., 2006; Schüller et al., 2008; Yang et al., 2008) have shed light on the cells-of-origin (Schüller et al., 2008; Selvadurai et al., 2020; Yang et al., 2008), tumor-propagating cells (Read et al., 2009; Vanner et al., 2014; Ward et al., 2009; Zhang et al., 2019), and mechanisms of therapeutic resistance and relapse (Morrissy et al., 2016; Ocasio et al., 2019) of SHH MB. Given the availability of genetically tractable models and lack of effective targeted therapy for SHH MB, we employed functional genomics to discover *bona fide* tumor maintenance genes of SHH MB.

RESULTS

Insertional mutagenesis implicates potassium channels in medulloblastoma maintenance

To identify cancer maintenance drivers, we engineered an *in vivo* screening system using Lazy Piggy (LP), a hybrid transposon containing both SB and PB excision sequences flanking cargo capable of dysregulating gene expression. The LP transposon was engineered by inserting PB inverted terminal repeats (ITRs) medial to the SB ITRs of the T2/Onc2 transposon (**Figures 1A-C**). Depending on the transposon integration site, target gene expression can be activated or disrupted through murine stem cell virus (MSCV) promoter-splice donor (SD) elements and splice acceptor-polyadenylation signal (SA-pA) elements, respectively (Ding et al., 2005; Dupuy et al., 2005). SB transposase enables primary mobilization of the LP transposon from a donor concatemer into random genomic reintegration sites, with relocated transposons dysregulating gene expression. Subsequent activation of tamoxifen-inducible PB remobilizes and depletes insertion events by extracting the transposon and restoring normal gene function (**Figures S1A-B**). We spatially and temporally controlled the LP system by tissue-specific SB transposase expression and tamoxifen-inducible PB transposase, respectively. SB transposase mobilizes the hybrid LP transposon from chromosomal concatemers, with relocated transposons disrupting gene expression in cell lineages of interest. Subsequent activation of tamoxifen-inducible PB remobilizes and depletes insertion events by extracting the transposon, thereby restoring original gene function (**Figure 1B**). Initiation, passenger, and progression insertions in tumor cells are removed with no deleterious effect on clonal survival. In contrast, transposon remobilization from maintenance insertions is deleterious, thereby mitigating tumor maintenance. This process depletes insertion events that are non-essential for clonal survival, while enriching for maintenance driver insertions to enable the identification of optimal targets for therapy development (**Figure 1C**).

To identify genes involved in MB maintenance, we generated a LP-driven murine model of SHH MB (**Figures S1C-H**). Mice heterozygous for *Ptch1*, a negative regulator of the Shh pathway, sporadically develop MB with low latency (Goodrich et al., 1997). In *Ptch1*$^{+/-}$ mice, LP mutagenesis is lineage-restricted to neural progenitors of the developing mouse cerebellum by Nestin-driven SB transposase (*Nestin:Luc-SB100*) and temporally regulated by tamoxifen-inducible PB transposase (*Nestin-Cre; R26-LSL-mPB-ER*^{T2}). To account for donor chromosome insertion bias, we generated separate founder mice harboring LP concatemers on chromosomes 7 and 10. (**Figures S1C-D**).

LP mutagenesis generated a highly penetrant model of SHH MB, accelerating medulloblastomagenesis in quintuple transgenic mice (*Ptch1*$^{+/-}$*; Nestin:Luc-SB100*$^{+/-}$*; Lazy Piggy*$^{+/-}$*; Nestin-Cre*$^{+/-}$*; R26-LSL-mPB*$^{ERT2+/-}$) compared to *Ptch1*$^{+/–}$ mice or quadruple transgenic mice without the *Ptch1*$^{+/–}$ allele (*Nestin:Luc-SB100*$^{+/-}$*; Lazy Piggy*$^{+/-}$*; Nestin-Cre*$^{+/-}$*; R26-LSL-mPB*$^{ERT2+/-}$) (**Figure 2A**). Following tumor formation, low-dose tamoxifen partially depletes primary insertions by remobilizing cargo and restoring normal gene function. Remobilization of tumor-essential (i.e. maintenance) insertions leads to clonal depletion. Remobilization of initiator, progressor, and passenger insertions does not impact clonal survival and leads to enrichment of maintenance insertions. Transposon remobilization by low-dose tamoxifen does not alter the survival of quintuple mice (**Figure S2G**), as the small proportion of remobilizations depletes non-essential insertions and is not curative. We performed restriction-splink PCR (Largaespada and Collier, 2008; Uren et al., 2009) and gene-centric common insertion site (gCIS) analysis (Brett et al., 2011) to determine reintegration sites with and without secondary mobilization in tumors from quintuple transgenic mice with (TAM^{+}) or without tamoxifen (TAM^{-}) treatment (**Figures S2A-C**). Insertions in two potassium channel genes, *Kcnb1* and *Kcnh2,* were enriched in TAM^{+} mice (**Figures 2B** and **S2D-E**). Notably, differential gene expression analysis of bulk RNA sequencing (RNA-seq) from TAM^{+} and TAM^{-} tumors revealed upregulated expression of additional potassium channel genes in TAM^{+} tumors (**Figures 2C** and **S2F**). Thus, the LP screen implicates potassium channels as potential regulators of MB maintenance.

While the membrane localization and availability of pharmacological agents makes potassium channels attractive therapeutic targets (Fan and Huang, 2020; Huang and Jan, 2014; Pardo and Stühmer, 2014), it is critical to identify a potassium channel target with MB-specific function. *Kcnb1* knockout mice are hyperactive and prone to seizures (Speca et al., 2014). *KCNB1* mutations are implicated in epileptic encephalopathy (Torkamani et al., 2014) and neurodevelopmental disorders (de Kovel et al., 2017) in humans. KCNH2 is a critical mediator of cardiac action potentials and its dysfunction can result in fatal cardiac arrhythmias (Sanguinetti and Tristani-Firouzi, 2006). Given the important functions of KCNB1 and KCNH2 in normal physiology, we examined potassium channel expression in MB more broadly to identify additional targets. Differential gene expression analysis of RNA-seq of human MB and cerebellum (Northcott et al., 2012a) identified *KCNB2,* the human paralog of *Kcnb1*, as the top-ranked potassium channel which is at least five-fold overexpressed across all four MB subgroups. Furthermore, *KCNB2* is the most highly expressed potassium channel across SHH, Group 3, and Group 4 MB, the three subgroups with poorest prognosis which collectively account for ~90% of all MB (**Figure 2D-G**). While KCNB1 and KCNB2 share structural and functional similarities (**Figure 2H**), KCNB2 is not implicated in human disorders (de Kovel et al., 2017). Taken together, our integrated cross-species study leverages both LP functional genomics to highlight potassium channels as MB maintenance drivers and orthogonal expression analysis to identify KCNB2 as the potassium channel with highest potential for MB-specificity. Therefore, we investigated the function of KCNB2 in MB.

Kcnb2 is dispensable during normal mouse development

We first studied Kcnb2 knockout mice to determine its role during normal mouse development (**Figure 3A-F** and **S3A-F**). Kcnb2 knockout mice are viable (**Figure 3A**), fertile (**Figure 3D**), produced offspring at expected mendelian ratios (**Figure 3B**) and displayed no defects in development (**Figure S3A**), body weight at weaning (**Figure 3C**), or brain morphology (**Figure 3E** and **S3B**). We observed no overt differences in the cerebellar architecture of Kcnb2 knockout mice at postnatal day 7 and 30 (P7 and P30) (**Figure 3F** and **S3C-F**). These data show that Kcnb2 is non-essential for normal mouse development.

Kcnb2 is overexpressed in mouse SHH MB and regulates tumor progression

To determine the role of Kcnb2 in MB, we used the *Math1-Cre; SmoM2* genetic mouse model of SHH MB. SmoM2 is a constitutively active form of Smoothened, a key SHH signaling component (Mao et al., 2006). Cre recombination in Math1-lineage cerebellar granule neuron progenitors, the SHH MB cell-of-origin, drives aberrant Shh signaling leading to aggressive brain tumors that recapitulate transcriptional and histopathological features of human SHH MB (Schüller et al., 2008; Yang et al., 2008). Kcnb2 deficiency prolongs the survival of MB-bearing mice in an allelic dose-dependent manner, and Kcnb2 homozygous knockout results in a 50% improvement in survival accompanied by markedly reduced tumor burden compared to control MB-bearing mice (**Figure 3G-H**). All *Math1-Cre; SmoM2; Kcnb2*$^{-/-}$ mice developed MBs, indicating that Kcnb2 does not regulate tumor initiation.

Intratumoral heterogeneity in SHH MB is driven by hierarchically organized tumor cell types. Sox2^{+} or Olig2^{+} medulloblastoma-propagating cells (MPCs) are slow-cycling and resistant to anti-mitotic chemotherapy (Vanner et al., 2014; Zhang et al., 2019). Sox2^{+} MPCs give rise to Dcx^{+} transit-amplifying progenitor cells, which divide and differentiate into NeuN^{+} post-mitotic tumor cells (Vanner et al., 2014). Due to these properties, MPCs are a source of MB relapse and a Sox2^{+} gene signature portends poor prognosis in SHH MB patients (Vanner et al., 2014). We performed single molecule *in situ* hybridization and found that *Kcnb2* colocalizes with *Sox2*$^{+}$ as well as *Dcx*$^{+}$ cells in *Math1-Cre; SmoM2* tumors (**Figure 3I**). Furthermore, *KCNB2* was detected in two independent single cell RNA sequencing datasets of human SHH MB containing a total of fourteen patient samples (Hovestadt et al., 2019; Riemondy et al., 2021). Consistently, we observed co-expression of *KCNB2* with *SOX2* and *DCX* in human SHH MB (**Figure 3J-K**), raising the possibility that Kcnb2 regulates Sox2^{+} MPCs.

Kcnb2 is required for tumor stage-dependent proliferative expansion of MPCs

We performed a series of pulse-chase experiments to investigate the label-retention properties of MPCs. The thymidine analogue BrdU is incorporated into DNA during S-phase and diluted upon serial cell divisions. To determine long-term MB cell cycle dynamics, BrdU was administered to tumor-bearing mice and analyzed following chase durations ranging from 1 to 14 days (**Figure S5A**). By quantifying BrdU label retention in distinct tumor populations, we found that Sox2^{+} MPCs are largely quiescent and label-retaining over the 14-day chase period (**Figure S5B** and **S5D**). Fast-cycling Dcx^{+} cells rapidly acquired and lost BrdU labelling (**Figure S5B** and

S5E). Postmitotic NeuN$^+$ cells are initially unlabeled, but NeuN$^+$; BrdU$^+$ cells slowly emerged concomitant with the decline of Dcx$^+$; BrdU$^+$ cells (**Figure S5B** and **S5F**), suggesting that NeuN$^+$ cells inherited BrdU from differentiated Dcx$^+$ cells. Therefore, our characterization of the quiescent, long-term label-retaining properties of Sox2$^+$ cells, and lineage relationship between Dcx$^+$ and NeuN$^+$ cells in *Math1-Cre; SmoM2* MBs are consistent with findings from the *Ptch1*$^{+/-}$ model of SHH MB (Vanner et al., 2014). As *PTCH1* and *SMO* are the most commonly mutated genes in human SHH MB (Kool et al., 2014), we conclude that MPC hierarchy is conserved in MB driven by distinct alterations in the SHH signaling pathway. Kcnb2 loss does not impact label retention dynamics of tumor cell types within the SHH MB hierarchy (**Figure S5C-F**), indicating that Kcnb2 knockout does not skew the Sox2$^+$ hierarchy towards ectopic fates.

Next, we examined whether reduced tumor burden due to Kcnb2 loss is associated with alteration of Sox2$^+$ MPCs. Since control MB-bearing mice display a median survival of 22 days, we examined the consequence of Kcnb2 knockout at early (P7) and late (P21) stages of MB tumorigenesis. In early-stage tumors, Kcnb2 knockout does not alter the number of MPCs (**Figure S4A**). In contrast, late-stage Kcnb2 knockout tumors display significantly fewer Sox2$^+$ MPCs compared to control (**Figure 4A**). The reduced Sox2$^+$ population was not attributable to apoptosis, as we did not detect differences in either apoptotic Sox2$^+$ MPCs or tumor cells overall (**Figure S4E-G**). While the overall tumor mitotic index was comparable (**Figure S4C-D**), we observed stage-specific changes in the cycling status of Sox2$^+$ MPCs (**Figure 4C-F**). In control tumors, the fraction of Ki67$^+$; Sox2$^+$ cycling MPCs decreased with tumor progression (P7 to P21; **Figure 4C-D**). Kcnb2 knockout diminishes MPC proliferation in early-stage (P7) MB (**Figure 4C-D**). At later stages (P21), both genotypes have comparably low levels MPC cycling (**Figure 4D**), consistent with a previous study that described the rapid proliferation of MPCs at SHH MB onset and transition towards quiescence in full-blown tumors (Zhang et al., 2019). These data demonstrate that Kcnb2 loss impairs the proliferative expansion of MPCs that occurs at early-stage MB.

To determine MPC cell cycle dynamics, MB-bearing mice were injected with BrdU and harvested 24 hours later (**Figure 4E**). By BrdU/Ki67 co-staining we found that P21 Sox2$^+$ MPCs display significantly increased cell cycle retention compared to their P7 counterparts (**Figure 4E**). Consistent with Kcnb2 knockout not affecting the already-diminished proliferation of P21 MPCs (**Figure 4D**), cell cycle retention at P21 was not changed upon loss of Kcnb2 (**Figure 4E**). However, Kcnb2 knockout P7 MPCs display increased cell cycle retention compared to control (**Figure 4E**), indicative of an elongated cell cycle. BrdU/PCNA co-staining revealed that specifically, Kcnb2 knockout increases S-phase retention in P7 MPCs (**Figure 4F**). Collectively, these data show that in control MB, Sox2$^+$ MPCs are more proliferative and undergo faster cell cycling during early tumor stages (P7) compared to later tumor stages (P21). Kcnb2 loss impairs this tumor stage-dependent proliferative expansion of the MPC pool by inducing S-phase retention and delaying cell cycle exit. Kcnb2 knockout does not impact the proliferation of transit-amplifying Dcx$^+$ MB cells (**Figure 4G-H**), and leads to only a minor, and likely biologically insignificant increase in Dcx$^+$ cell cycle retention (**Figure 4I**). Given that Kcnb2 knockout induces much stronger

cell cycle defects in early stage Sox2$^+$ MPCs, and their position atop the SHH MB hierarchy, we focused on determining the mechanism of Kcnb2 function in P7 Sox2$^+$ MPCs.

Kcnb2 regulates potassium homeostasis and mechanical properties of MPCs

To determine the mechanism by which Kcnb2 regulates MPCs, we isolated Sox2$^+$ cells from MB (Huang et al., 2010). Consistent with their *in vivo* defects, Kcnb2 knockout MPCs isolated from P7 mice display impaired *in vitro* growth (**Figure 5A**), as well as primary and secondary sphere-forming capacity (**Figure 5B**). We performed whole-cell patch clamp recordings to compare potassium channel activity in MPCs. Currents were elicited by voltage steps from -80 to 80 mV in 20-mV increments. Kcnb2 knockout MPCs display reduced potassium currents (**Figure 5C-D**). Administration of 4-Aminopyridine (4-AP), a blocker of voltage-gated potassium currents, to control MPCs phenocopies the knockout-induced sphere-forming defects (**Figure 5B**). These results indicate that Kcnb2-mediated potassium currents govern MPC proliferation in a cell-autonomous manner. Due to the higher intracellular potassium concentration, potassium channel opening causes potassium efflux along its electrochemical gradient. We postulate that Kcnb2 loss leads to elevated intracellular potassium, resulting in increased intracellular osmolarity to cause water influx and cell swelling. Consistent with this notion, Kcnb2 knockout MPCs display increased membrane capacitance (**Figure 5E**), which is proportional to the surface area of the plasma membrane (Hille, 2001). Furthermore, Kcnb2 knockout MPCs develop larger cell size compared to control, as assessed by immunofluorescence for SmoM2-YFP (**Figure 5F**).

Given that Kcnb2 knockout impacts MPC size and plasma membrane surface area, we next investigated whether cell mechanics were impacted. Increased intracellular potassium due to Kcnb2 knockout and subsequent water influx may increase inner cell pressure, a force pushing outward against the plasma membrane. Plasma membrane constriction and expansion impact membrane tension (the in-plane force which counteracts surface expansion), a biophysical parameter that regulates cell fate specification (Bergert et al., 2020; De Belly et al., 2020). Therefore, we examined these two biomechanical parameters: membrane tension and inner cell pressure (**Figure 5G**). Using atomic force microscopy coupled with a sharp probe to induce small, local indentations, we found that Kcnb2 knockout reduces the plasma membrane tension of MPCs (**Figure 5H**). We determined inner cell pressure using micropipette aspiration, where a negative pressure is applied to MPCs. Inner cell pressure, which generates a rounding force to resist cell deformation, is inversely proportional to the amount of cell being aspirated into the micropipette. Kcnb2 knockout did not alter MPC inner cell pressure (**Figure 5I**), indicating that osmolarity-driven water influx and cell swelling may be compensated by modulating membrane tension. Broad inhibition of potassium currents with tetraethylammonium (TEA), a general potassium channel blocker, or inhibition of voltage-gated potassium currents with 4-AP increased cell size while reducing plasma membrane tension (**Figure 5J-L**). Taken together, these data show that Kcnb2-dependent potassium homeostasis regulates MPC proliferation, cell size, and plasma membrane tension.

Kcnb2 regulates plasma membrane-actin cortex tethering of MPCs

Next, we investigated the mechanism by which Kcnb2 regulates plasma membrane tension. When cell size increases, plasma membrane remodels to ensure that the mechanically inflexible lipid bilayer does not rupture due to cell swelling. Plasma membrane-to-actin cortex tethering by ERM (Ezrin, Radixin, Moesin) proteins is a key contributing factor to cell surface mechanics, including membrane tension. Phosphorylation of ERM (pERM) induces an open conformation permissive to binding F-actin (Fehon et al., 2010). pERM membrane tethering sequesters membrane surface area to increase tension, whereas reduced pERM increases the amount of untethered membrane free to unfold in response to osmotic changes. We investigated if Kcnb2 regulates pERM membrane-actin tethering and membrane tension through changes in osmolarity, and tested whether manipulating extracellular osmolarity rescues changes in cell size and plasma membrane-actin tethering (**Figure 6A**). Under isotonic conditions, Kcnb2 knockout reduced pERM tethering of MPCs between the plasma membrane and the actin cytoskeleton, concomitant with increased cell size (**Figure 6B-C**) and decreased overall pERM protein (**Figure S6B**).

Control MPCs in hypotonic media phenocopies Kcnb2 knockout, with cell swelling and reduced pERM tethering. However, hypertonic media failed to further shrink or increase membrane-actin tethering in control MPCs (**Figure 6B-C**). The enlarged cell size and reduced pERM tethering of Kcnb2 knockout MPCs is rescued by hypertonic conditions, which reduces cell size and increases membrane tethering. Conversely, while hypotonic conditions are able to further enlarge the already-swollen Kcnb2 knockout MPCs, this is not accompanied by further reduction in pERM tethering (**Figure 6B-C**). These data suggest that Kcnb2 maintains potassium and cell volume homeostasis to regulate MPC membrane tension through pERM-mediated membrane-actin tethering (**Figure 6D**). Membrane tension and pERM tethering rise as cells undergo mitosis to facilitate mitotic cell rounding and proper positioning of mitotic spindles by the tethered actin cortex (Fehon et al., 2010; Raucher and Sheetz, 1999). The proliferation defects and lengthened cell cycle observed in Kcnb2 knockout MPCs (**Figure 4C-F**) may be attributed to reduced MPC membrane tension and pERM tethering. The osmolarity manipulations suggest that osmotic regulation of cell size and membrane tension are regulated and coupled within a physiological range. Control Sox2^{+} MPCs are already quite small with very little cytoplasm, hindering further reduction in cell size. While hypotonic conditions can further increase the size of Kcnb2 knockout MPCs, coupling between cell size and pERM tethering breaks down, as further reduction of membrane tethering at large cell sizes may lead to membrane rupture.

Kcnb2 regulates EGFR endocytosis through membrane tension

We sought to determine how membrane tension regulates MPC proliferation. Membrane tension serves as an energy barrier that gates biological processes involving membrane folding, such as endocytosis. A more flexible plasma membrane and reduced membrane tension facilitate endocytosis (Dai and Sheetz, 1995; De Belly et al., 2020; Thottacherry et al., 2018). Endocytosis occurs mainly through clathrin- and caveolae-dependent pathways, where membrane domains to be internalized are encased by Clathrin and Caveolin-1, respectively. Kcnb2

knockout MPCs display increased Caveolin-1$^+$ and Clathrin$^+$ puncta, as well as increased Rab5$^+$ puncta, a marker of early endosomes (**Figure 6E, 6G**). Endocytosis of receptor tyrosine kinases regulates signaling output (Sigismund et al., 2021). Brain tumor-propagating cells are traditionally maintained with epidermal growth factor (EGF) and fibroblast growth factor (FGF), both of which activate receptor tyrosine kinases (Pollard et al., 2009). Through a series of growth factor titrations, we found that MPC viability is crucially dependent on EGF but not FGF (**Figure S6A**). Kcnb2 knockout MPCs display reduced amounts of activated phosphorylated EGFR (**Figures 6F-G** and **S6B**), accompanied by increased colocalization of pEGFR$^+$ and Caveolin-1$^+$ puncta (**Figure 6H**). Total internal reflection fluorescence (TIRF) microscopy, which specifically visualizes plasma membrane-localized proteins, further validated the increased Caveolin-1$^+$ endocytic puncta and decreased levels of membrane-localized pEGFR in Kcnb2 knockout MPCs (**Figure 6I**). These data suggest that reduced membrane tension increases internalization of EGFRs through endocytosis in Kcnb2 knockout MPCs. We corroborated our results by immunohistochemistry of Sox2$^+$ MPCs in early-stage (P7) *Math1-Cre; SmoM2* tumors. Consistently, Kcnb2 knockout MPCs display reduced pERM, increased Caveolin-1, and reduced pEGFR signal compared to control (**Figure 7A-B**), consistent with our *in vitro* observations.

We next manipulated membrane tension to establish causality between membrane tension, endocytosis, and EGFR signaling (**Figure 7C**). NSC668394, an inhibitor of Ezrin phosphorylation, reduces plasma membrane-to-actin cortex tethering and membrane tension (Bulut et al., 2012; De Belly et al., 2020). Methyl-β-cyclodextrin (MβCD) depletes cholesterol from the plasma membrane, reduces endocytosis, and increases membrane tension (Biswas et al., 2019; De Belly et al., 2020; Rodal et al., 1999). Treating control MPCs with NSC668394 increases cell size, elevates Caveolin-1 expression, and reduces pEGFR levels, mimicking the Kcnb2 knockout phenotype (**Figure 7D**). Conversely, treating Kncb2 knockout MPCs with MβCD reduces cell size, decreases Caveolin-1 expression, and increases pEGFR levels (**Figure 7E**). These data establish membrane tension as a regulator of endocytosis and EGFR signaling in MPCs.

Ionic homeostasis and membrane tension govern EGFR signaling and proliferation in MB

Next, we asked whether manipulating the membrane tension–EGFR axis can rescue the proliferation defect of Kncb2 knockout MPCs. Relative to control, Kncb2 knockout MPCs have lower BrdU incorporation *in vitro* (**Figure 7F**). Decreased EGF concentration (from 10 ng/mL to 1 ng/mL) reduces BrdU incorporation in control MPCs to a similar extent as Kcnb2 knockout. Supplementation with EGF ligand rescues the BrdU incorporation rate of Kcnb2 knockout MPCs to control levels. Combination of EGF and MβCD further increases BrdU incorporation, suggesting that high membrane tension cooperates with EGF ligands to facilitate MPC proliferation (**Figure 7F**).

Finally, since we did not observe any developmental or physiological phenotypes in Kcnb2 knockout mice (**Figure 3A-F** and **S3A-F**), and Sox2$^+$ MPCs are refractory to anti-SHH signaling therapies (Vanner et al., 2014), we determined whether Kcnb2 knockout synergizes with SHH pathway antagonism to treat SHH MB. Vismodegib, a small-molecule Shh signaling pathway antagonist, is approved for treating SHH signaling-driven

basal cell carcinoma and undergoing clinical trials for recurrent SHH MB (Li et al., 2019). We administered three daily doses of vismodegib or vehicle to MB-bearing mice (**Figure 7G**). Vismodegib treatment alone did not improve the survival of control MB-bearing mice compared to vehicle treatment, consistent with a previous report (Ocasio et al., 2019). In contrast, vismodegib treatment significantly prolonged the survival of Kcnb2 knockout MB-bearing mice. These data establish Kcnb2 as a target for the therapy-resistant MPCs, underscoring a synergism between Kcnb2 inhibition and tumor-debulking agents in treating SHH MB.

DISCUSSION

A major obstacle in treating cancer is the ever-changing therapeutic vulnerabilities in space and time. Tumor evolution, which invariably occurs under the stress from tumor cells and their microenvironment, frequently nullifies tumor dependencies on initiation mutations while developing new dependencies that maintain the growing tumor. As a result, identifying mechanisms that maintain, rather than initiate, tumors are of tremendous clinical significance. Most cancer genomics studies are designed to identify tumor initiation events, leaving tumor maintenance underpinnings unexplored. In this study, we designed the Lazy Piggy insertional mutagenesis system to identify maintenance mechanisms of MB. In a genetic mouse model of MB, SB first mobilizes the hybrid transposon to disrupt gene expression. Subsequent PB activation depletes SB insertions, thereby restoring original gene function. Under these genomic manipulations, initiation, passenger, and progression insertions are removed with no effect on tumor survival. In contrast, removing maintenance insertions leads to clonal collapse. Therefore, Lazy Piggy functional genomics filters out initiation, passenger, and progression genes, while revealing the maintenance mechanisms. This represents the first *in vivo* functional genomics tool designed to uncover tumor maintenance events.

Using this novel insertional mutagenesis approach, we identify potassium homeostasis as a critical dependency of MB. *KCNB2* is the most consistently upregulated potassium channel across all four MB subgroups. While Kcnb2 is non-essential for normal mouse development, Kcnb2 knockout markedly hinders MB growth and prolongs survival of tumor-bearing mice. Kcnb2 expression is enriched in the therapy-resistant Sox2$^+$ MPCs, and Kcnb2 loss diminishes the MPC pool by impairing its tumor stage-dependent proliferative expansion. Mechanistically, Kcnb2 maintains MPC cell size and governs the mechanical properties of plasma membrane, which in turn gates endocytosis-regulated EGFR signaling (**Figure 7H**). Plasma membrane tension is a tightly controlled biomechanical property which governs cell behaviors such as migration and division (Sitarska and Diz-Muñoz, 2020). In embryonic stem cells, reduction of membrane tension is an essential step in differentiation and pluripotency exit (Bergert et al., 2020; De Belly et al., 2020). Here, our study establishes Kcnb2 as a vulnerability in MB maintenance and provides the first evidence that ionic homeostasis-gated membrane tension is critical for tumor-propagating cell proliferation and tumor progression. Furthermore, we show that targeting Kcnb2 synergizes with tumor debulking chemotherapies to impair MB growth.

Osmotic stress is a physiologically relevant force which cells must adapt and respond to. The relatively inextensible plasma membrane can only sustain 3-4% stretch before membrane rupture (Nichol and Hutter, 1996), and thus membrane tension must be maintained at sub-lytic levels to prevent cell lysis. In this study, we found that Kcnb2 knockout in MPCs leads to hypotonic cell swelling (**Figure 5F**) and reduced membrane tension (**Figure 5H**). This contrasts with previous studies reporting that membrane tension spikes within seconds of acute hypotonic cell swelling, followed by recovery of both volume and tension on a timescale of minutes to hours (Dai et al., 1998; Roffay et al., 2021). Excess membrane is stored as cell surface reservoirs of protrusions and invaginations, maintained by cytoskeleton-membrane tethering (Welf et al., 2020). The initial transient tension increase reflects an inability to rapidly provide excess membrane and counterbalance the increased cell volume (Pietuch et al., 2013). Cells then responds to hypotonic swelling by cytoskeletal reorganization to release tethered membrane surface area and drive membrane unfolding (Roffay et al., 2021). Finally, recovery from hypotonic swelling is mediated by ion channels and transporters which efflux osmolytes from cells to reduce volume. Being the major intracellular cation class, potassium has a dominant influence in establishing electrochemical equilibrium. Global and constitutive Kcnb2 loss from MPCs leads to reduced outward potassium currents (**Figure 5C-D**) and increased cell size (**Figure 5F**), indicating that compensatory mechanisms are not sufficient to rescue the perturbed potassium homeostasis. Since Kcnb2 knockout MPCs remain larger than control, our data suggest that the membrane reservoirs remain depleted, cytoskeleton-membrane tethering and membrane refolding cannot occur, thus resulting in decreased membrane tension.

Previous studies of extrinsic osmotic shock and membrane tension reflect acute and transient cellular adaptations to hypotonic swelling in cells with intact volume regulatory machinery (Dai et al., 1998; Pietuch et al., 2013; Roffay et al., 2021). Our study differs in three critical aspects. First, we induced osmotic shock in a cell-autonomous manner by knocking out the endogenously overexpressed potassium channel Kcnb2. Second, we describe the chronic effects of dysregulated potassium homeostasis on membrane tension in cells unable to re-establish their original ionic balance and cell volume. Finally, intrinsic differences between the various cell types studied must be taken into consideration. The prior studies used *Lymnaea* molluscan neurons, Madin Darby canine kidney (MDCK II) cells, and HeLa Kyoto cancer cells respectively (Dai et al., 1998; Pietuch et al., 2013; Roffay et al., 2021), while our mechano-osmotic experiments were performed in murine brain tumor cells. While these studies all provide critical insights into the interplay between osmoregulation and mechanobiology, the cell-intrinsic differences preclude comparisons across species.

While specific ion channels are overexpressed in cancer, their expression in non-malignant tissues is tightly regulated, providing a therapeutic window to target ion channels in cancer (Fan and Huang, 2020). While calcium is a well-established second messenger that engages intracellular signaling, how other cations such as potassium influence mechano-chemical signaling was unclear. Our study reveals how potassium homeostasis regulates plasma membrane-actin cortex tethering and cell surface mechanics. Decreased membrane tension enhances endocytosis, which enhances internalization of membrane-localized signaling molecules such as

EGFR and attenuates the signaling output. Since membrane tension reduction leads to a more 'pliable' plasma membrane, we emphasize the possibility that the membrane tension drop we observe in Kcnb2 knockout BTICs creates a permissive environment for other processes dependent on plasma membrane remodeling, such as pinocytosis and exocytosis. While we implicate EGFR signaling as a functionally relevant consequence of Kcnb2 knockout-induced endocytosis, EGFR is likely not the sole membrane protein affected by alterations in plasma membrane tension.

Lastly, our study reveals that osmolarity influences plasma membrane tension. MB, as many other tumor types, develops extensive intratumoral heterogeneity. Our study raises the possibility that microenvironment-dependent differences in extracellular osmolarity may dictate membrane tension and tumor cell behavior. The extracellular osmotic environment in MB can differ depending on whether tumor cells are exposed to cerebrospinal fluid near the brain ventricles, plasma near leaky blood vessels, or interstitial fluid in the densely packed tumor core. An intriguing question is whether distinct membrane tension levels arise in tumor cells situated in anatomically different tumor regions, and whether potassium channels integrate osmotic and mechanical heterogeneity to regulate functional plasticity in stemness, lineage bias, and therapy resistance. Potassium homeostasis-governed biophysical properties of cancer represent therapeutic avenues to halt tumor progression.

LIMITATIONS OF THE STUDY

Functional cancer genomics enables the identification of genes which may be missed by expression analysis. However, *in vivo* genomic approaches may not distinguish between tumor-essential and pan-essential genes, with the latter resulting in a limited therapeutic index. Conversely, differential expression analysis may yield tumor-specific targets that require functional validation. We partially circumvented this limitation by focusing on enriched pathways to reveal convergence on the potassium channel family as mediators of MB maintenance, and through analysis of MB patient expression data identify KCNB2 as the most consistently upregulated potassium channel in MB. A limitation of our study is the small sample size of Lazy Piggy tumors, which may have contributed to the discordant identification of KCNB2 from patient expression analysis but not the Lazy Piggy screen. Further studies using the Lazy Piggy model will require a larger cohort to increase genomic coverage of transposon mobilization and remobilization to discover new tumor maintenance drivers.

ACKNOWLEDGEMENTS

This work is supported by Sontag Foundation Distinguished Scientist Award, Early Researcher Award, Canadian Cancer Society Challenge Grant, Cancer Research Society Operating Grant, Natural Sciences and Engineering Research Council Discovery Grant, American Brain Tumor Association Discovery Grant, Ontario Institute for Cancer Research Translational Research Initiative, Canadian Institute of Health Research Project Grants, b.r.a.i.n.child, and Meagan's HUG to X.H. and National Institutes of Health grants CA148699 and CA159859, Stand Up To Cancer (SU2C) St. Baldrick's Pediatric Dream Team translational research grant (SU2C-AACR-DT1113) and SU2C Canada Cancer Stem Cell Dream Team research funding (SU2C-AACR-DT-19-15) provided

by the Government of Canada through Genome Canada and the Canadian Institutes of Health Research, with supplementary support from the Ontario Institute for Cancer Research through funding provided by the Government of Ontario to M.D.T. SU2C is a program of the Entertainment Industry Foundation administered by American Association for Cancer Research. M.D.T. is also supported by Pediatric Brain Tumor Foundation, Terry Fox Research Institute, Canadian Institutes of Health Research, Cure Search Foundation, b.r.a.i.n.child, Meagan's Walk, SWIFTY Foundation, Brain Tumour Charity, Genome Canada, Genome BC, Genome Quebec, Ontario Research Fund, Worldwide Cancer Research, V-Foundation for Cancer Research, and Ontario Institute for Cancer Research through funding provided by the Government of Ontario. Additionally, M.D.T. is supported by Canadian Cancer Society Research Institute Impact grant, Cancer Research UK Brain Tumour Award, Garron Family Chair in Childhood Cancer Research at The Hospital for Sick Children, and University of Toronto. J.J.F. is supported by Restracomp Scholarship from The Hospital for Sick Children. X.W. is supported by Lap-Chee Tsui Fellowship from The Hospital for Sick Children and Dunn with Cancer Research Fellowship from Brain Tumour Foundation of Canada. X.C. is supported by Restracomp Fellowship from The Hospital for Sick Children. S.B. is supported by International Postdoc Grant from Swedish Research Council. N.A. is supported by Childhood Cancer Research Postdoctoral Fellow Grant from Rally Foundation and Restracomp Fellowship from The Hospital for Sick Children. We thank Paul Paroutis and Kimberly Lau at SickKids Imaging Facility for help with confocal imaging and image analysis. Schematics were created using BioRender. X.H. thanks the love and support from Lucas Huang and Liam Huang. X.H. is a Catalyst Scholar at The Hospital for Sick Children and Canada Research Chair in Cancer Biophysics.

AUTHOR CONTRIBUTIONS

J.J.F. performed all mouse work and wet laboratory experiments; Xin W. generated and performed validation experiments of the LP mouse; P.S. and A.W.E. were responsible for LP bioinformatic analysis; Xian W. performed membrane tension measurements; G.S. performed micropipette aspiration experiments; X.C. performed electrophysiology experiments and assisted with mouse work; Y.X., S.W., H.F., and A.S.M. assisted with bioinformatic analysis; S.B., M.A.F., R.J.P., and N.A. assisted with mouse work; all other authors contributed to methodology development and reagents. J.J.F. and A.W.E. wrote the manuscript with input from all other authors; X.H. and M.D.T. conceived and supervised the project.

DECLARATION OF INTEREST

The authors declare no competing financial interests.

REFERENCES

Alquicira-Hernandez, J., and Powell, J.E. (2021). *Nebulosa* recovers single-cell gene expression signals by kernel density estimation. Bioinformatics *37*, 2485–2487. https://doi.org/10.1093/bioinformatics/btab003.

Beckmann, P.J., Larson, J.D., Larsson, A.T., Ostergaard, J.P., Wagner, S., Rahrmann, E.P., Shamsan, G.A., Otto, G.M., Williams, R.L., Wang, J., et al. (2019). Sleeping Beauty Insertional Mutagenesis Reveals Important Genetic Drivers of Central Nervous System Embryonal Tumors. Cancer Res *79*, 905–917. https://doi.org/10.1158/0008-5472.CAN-18-1261.

Bergert, M., Lembo, S., Sharma, S., Russo, L., Milovanović, D., Gretarsson, K.H., Börmel, M., Neveu, P.A., Hackett, J.A., Petsalaki, E., et al. (2020). Cell Surface Mechanics Gate Embryonic Stem Cell Differentiation. Cell Stem Cell S1934590920305336. https://doi.org/10.1016/j.stem.2020.10.017.

Biswas, A., Kashyap, P., Datta, S., Sengupta, T., and Sinha, B. (2019). Cholesterol Depletion by MβCD Enhances Cell Membrane Tension and Its Variations-Reducing Integrity. Biophys J *116*, 1456–1468. https://doi.org/10.1016/j.bpj.2019.03.016.

Brett, B.T., Berquam-Vrieze, K.E., Nannapaneni, K., Huang, J., Scheetz, T.E., and Dupuy, A.J. (2011). Novel Molecular and Computational Methods Improve the Accuracy of Insertion Site Analysis in Sleeping Beauty-Induced Tumors. PLoS ONE *6*, e24668. https://doi.org/10.1371/journal.pone.0024668.

Bulut, G., Hong, S.-H., Chen, K., Beauchamp, E.M., Rahim, S., Kosturko, G.W., Glasgow, E., Dakshanamurthy, S., Lee, H.-S., Daar, I., et al. (2012). Small molecule inhibitors of ezrin inhibit the invasive phenotype of osteosarcoma cells. Oncogene *31*, 269–281. https://doi.org/10.1038/onc.2011.245.

Cadiñanos, J., and Bradley, A. (2007). Generation of an inducible and optimized piggyBac transposon system†. Nucleic Acids Research *35*, e87. https://doi.org/10.1093/nar/gkm446.

Chen, X., Wanggou, S., Bodalia, A., Zhu, M., Dong, W., Fan, J.J., Yin, W.C., Min, H.-K., Hu, M., Draghici, D., et al. (2018). A Feedforward Mechanism Mediated by Mechanosensitive Ion Channel PIEZO1 and Tissue Mechanics Promotes Glioma Aggression. Neuron *100*, 799-815.e7. https://doi.org/10.1016/j.neuron.2018.09.046.

Dai, J., and Sheetz, M.P. (1995). Regulation of Endocytosis, Exocytosis, and Shape by Membrane Tension. Cold Spring Harb Symp Quant Biol *60*, 567–571. https://doi.org/10.1101/SQB.1995.060.01.060.

Dai, J., Sheetz, M.P., Wan, X., and Morris, C.E. (1998). Membrane Tension in Swelling and Shrinking Molluscan Neurons. J Neurosci *18*, 6681–6692. https://doi.org/10.1523/JNEUROSCI.18-17-06681.1998.

De Belly, H., Stubb, A., Yanagida, A., Labouesse, C., Jones, P.H., Paluch, E.K., and Chalut, K.J. (2020). Membrane Tension Gates ERK-Mediated Regulation of Pluripotent Cell Fate. Cell Stem Cell S1934590920305348. https://doi.org/10.1016/j.stem.2020.10.018.

Ding, S., Wu, X., Li, G., Han, M., Zhuang, Y., and Xu, T. (2005). Efficient Transposition of the piggyBac (PB) Transposon in Mammalian Cells and Mice. Cell *122*, 473–483. https://doi.org/10.1016/j.cell.2005.07.013.

Dobin, A., Davis, C.A., Schlesinger, F., Drenkow, J., Zaleski, C., Jha, S., Batut, P., Chaisson, M., and Gingeras, T.R. (2013). STAR: ultrafast universal RNA-seq aligner. Bioinformatics *29*, 15–21. https://doi.org/10.1093/bioinformatics/bts635.

Dupuy, A.J., Akagi, K., Largaespada, D.A., Copeland, N.G., and Jenkins, N.A. (2005). Mammalian mutagenesis using a highly mobile somatic Sleeping Beauty transposon system. Nature *436*, 221–226. https://doi.org/10.1038/nature03691.

Eil, R., Vodnala, S.K., Clever, D., Klebanoff, C.A., Sukumar, M., Pan, J.H., Palmer, D.C., Gros, A., Yamamoto, T.N., Patel, S.J., et al. (2016). Ionic immune suppression within the tumour microenvironment limits T cell effector function. Nature *537*, 539–543. https://doi.org/10.1038/nature19364.

Fan, J.J., and Huang, X. (2020). Ion Channels in Cancer: Orchestrators of Electrical Signaling and Cellular Crosstalk. (Berlin, Heidelberg: Springer Berlin Heidelberg), p.

Fehon, R.G., McClatchey, A.I., and Bretscher, A. (2010). Organizing the cell cortex: the role of ERM proteins. Nature Reviews Molecular Cell Biology *11*, 276–287. https://doi.org/10.1038/nrm2866.

Francisco, M.A., Wanggou, S., Fan, J.J., Dong, W., Chen, X., Momin, A., Abeysundara, N., Min, H.-K., Chan, J., McAdam, R., et al. (2020). Chloride intracellular channel 1 cooperates with potassium channel EAG2 to promote medulloblastoma growth. Journal of Experimental Medicine *217*, e20190971. https://doi.org/10.1084/jem.20190971.

Genovesi, L.A., Ng, C.G., Davis, M.J., Remke, M., Taylor, M.D., Adams, D.J., Rust, A.G., Ward, J.M., Ban, K.H., Jenkins, N.A., et al. (2013). Sleeping Beauty mutagenesis in a mouse medulloblastoma model defines networks that discriminate between human molecular subgroups. Proceedings of the National Academy of Sciences *110*, E4325–E4334. https://doi.org/10.1073/pnas.1318639110.

Goodrich, L.V., Milenković, L., Higgins, K.M., and Scott, M.P. (1997). Altered Neural Cell Fates and Medulloblastoma in Mouse *patched* Mutants. Science *277*, 1109–1113. https://doi.org/10.1126/science.277.5329.1109.

Hao, Y., Hao, S., Andersen-Nissen, E., Mauck, W.M., Zheng, S., Butler, A., Lee, M.J., Wilk, A.J., Darby, C., Zager, M., et al. (2021). Integrated analysis of multimodal single-cell data. Cell *184*, 3573-3587.e29. https://doi.org/10.1016/j.cell.2021.04.048.

Hermanstyne, T.O., Kihira, Y., Misono, K., Deitchler, A., Yanagawa, Y., and Misonou, H. (2010). Immunolocalization of the voltage-gated potassium channel Kv2.2 in GABAergic neurons in the basal forebrain of rats and mice. J. Comp. Neurol. *518*, 4298–4310. https://doi.org/10.1002/cne.22457.

Hille, B. (2001). Ion Channels of Excitable Membranes (Sunderland, Mass: Sinauer Associates is an imprint of Oxford University Press).

Hovestadt, V., Smith, K.S., Bihannic, L., Filbin, M.G., Shaw, M.L., Baumgartner, A., DeWitt, J.C., Groves, A., Mayr, L., Weisman, H.R., et al. (2019). Resolving medulloblastoma cellular architecture by single-cell genomics. Nature https://doi.org/10.1038/s41586-019-1434-6.

Huang, X., and Jan, L.Y. (2014). Targeting potassium channels in cancer. J Cell Biol *206*, 151–162. https://doi.org/10.1083/jcb.201404136.

Huang, X., Ketova, T., LItingtung, Y., and Chiang, C. (2010). Isolation, Enrichment, and Maintenance of Medulloblastoma Stem Cells. JoVE 2086. https://doi.org/10.3791/2086.

Jeong, J., Mao, J., Tenzen, T., Kottmann, A.H., and McMahon, A.P. (2004). Hedgehog signaling in the neural crest cells regulates the patterning and growth of facial primordia. Genes Dev *18*, 937–951. https://doi.org/10.1101/gad.1190304.

Johnston, D.L., Keene, D., Kostova, M., Lafay-Cousin, L., Fryer, C., Scheinemann, K., Carret, A.-S., Fleming, A., Percy, V., Afzal, S., et al. (2015). Survival of children with medulloblastoma in Canada diagnosed between 1990 and 2009 inclusive. J Neurooncol *124*, 247–253. https://doi.org/10.1007/s11060-015-1831-0.

Joshi, M., Keith Pittman, H., Haisch, C., and Verbanac, K. (2008). Real-time PCR to determine transgene copy number and to quantitate the biolocalization of adoptively transferred cells from EGFP-transgenic mice. Biotechniques *45*, 247–258. https://doi.org/10.2144/000112913.

Kas, S.M., de Ruiter, J.R., Schipper, K., Annunziato, S., Schut, E., Klarenbeek, S., Drenth, A.P., van der Burg, E., Klijn, C., ten Hoeve, J.J., et al. (2017). Insertional mutagenesis identifies drivers of a novel oncogenic pathway in invasive lobular breast carcinoma. Nat Genet *49*, 1219–1230. https://doi.org/10.1038/ng.3905.

Kawaguchi, A., Miyata, T., Sawamoto, K., Takashita, N., Murayama, A., Akamatsu, W., Ogawa, M., Okabe, M., Tano, Y., Goldman, S.A., et al. (2001). Nestin-EGFP Transgenic Mice: Visualization of the Self-Renewal and Multipotency of CNS Stem Cells. Molecular and Cellular Neuroscience *17*, 259–273. https://doi.org/10.1006/mcne.2000.0925.

Keng, V.W., Villanueva, A., Chiang, D.Y., Dupuy, A.J., Ryan, B.J., Matise, I., Silverstein, K.A.T., Sarver, A., Starr, T.K., Akagi, K., et al. (2009). A conditional transposon-based insertional mutagenesis screen for genes associated with mouse hepatocellular carcinoma. Nat Biotechnol *27*, 264–274. https://doi.org/10.1038/nbt.1526.

Kool, M., Jones, D.T.W., Jäger, N., Northcott, P.A., Pugh, T.J., Hovestadt, V., Piro, R.M., Esparza, L.A., Markant, S.L., Remke, M., et al. (2014). Genome Sequencing of SHH Medulloblastoma Predicts Genotype-Related Response to Smoothened Inhibition. Cancer Cell *25*, 393–405. https://doi.org/10.1016/j.ccr.2014.02.004.

Korsunsky, I., Millard, N., Fan, J., Slowikowski, K., Zhang, F., Wei, K., Baglaenko, Y., Brenner, M., Loh, P., and Raychaudhuri, S. (2019). Fast, sensitive and accurate integration of single-cell data with Harmony. Nat Methods *16*, 1289–1296. https://doi.org/10.1038/s41592-019-0619-0.

de Kovel, C.G.F., Syrbe, S., Brilstra, E.H., Verbeek, N., Kerr, B., Dubbs, H., Bayat, A., Desai, S., Naidu, S., Srivastava, S., et al. (2017). Neurodevelopmental Disorders Caused by De Novo Variants in KCNB1 Genotypes and Phenotypes. JAMA Neurology *74*, 1228–1236. https://doi.org/10.1001/jamaneurol.2017.1714.

Largaespada, D.A., and Collier, L.S. (2008). Transposon-mediated mutagenesis in somatic cells: identification of transposon-genomic DNA junctions. Methods Mol Biol *435*, 95–108. https://doi.org/10.1007/978-1-59745-232-8_7.

Li, M.A., Pettitt, S.J., Eckert, S., Ning, Z., Rice, S., Cadiñanos, J., Yusa, K., Conte, N., and Bradley, A. (2013). The *piggyBac* Transposon Displays Local and Distant Reintegration Preferences and Can Cause Mutations at Noncanonical Integration Sites. Mol Cell Biol *33*, 1317–1330. https://doi.org/10.1128/MCB.00670-12.

Li, Y., Song, Q., and Day, B.W. (2019). Phase I and phase II sonidegib and vismodegib clinical trials for the treatment of paediatric and adult MB patients: a systemic review and meta-analysis. Acta Neuropathologica Communications *7*, 123. https://doi.org/10.1186/s40478-019-0773-8.

Love, M.I., Huber, W., and Anders, S. (2014). Moderated estimation of fold change and dispersion for RNA-seq data with DESeq2. Genome Biol *15*, 550. https://doi.org/10.1186/s13059-014-0550-8.

Mao, J., Ligon, K.L., Rakhlin, E.Y., Thayer, S.P., Bronson, R.T., Rowitch, D., and McMahon, A.P. (2006). A Novel Somatic Mouse Model to Survey Tumorigenic Potential Applied to the Hedgehog Pathway. Cancer Res *66*, 10171–10178. https://doi.org/10.1158/0008-5472.CAN-06-0657.

Matei, V., Pauley, S., Kaing, S., Rowitch, D., Beisel, K.W., Morris, K., Feng, F., Jones, K., Lee, J., and Fritzsch, B. (2005). Smaller inner ear sensory epithelia in Neurog 1 null mice are related to earlier hair cell cycle exit. Dev Dyn *234*, 633–650. https://doi.org/10.1002/dvdy.20551.

Mátés, L., Chuah, M.K.L., Belay, E., Jerchow, B., Manoj, N., Acosta-Sanchez, A., Grzela, D.P., Schmitt, A., Becker, K., Matrai, J., et al. (2009). Molecular evolution of a novel hyperactive Sleeping Beauty transposase enables robust stable gene transfer in vertebrates. Nat Genet *41*, 753–761. https://doi.org/10.1038/ng.343.

McInnes, L., Healy, J., and Melville, J. (2020). UMAP: Uniform Manifold Approximation and Projection for Dimension Reduction.

Moriarity, B.S., Otto, G.M., Rahrmann, E.P., Rathe, S.K., Wolf, N.K., Weg, M.T., Manlove, L.A., LaRue, R.S., Temiz, N.A., Molyneux, S.D., et al. (2015). A Sleeping Beauty forward genetic screen identifies new genes and pathways driving osteosarcoma development and metastasis. Nat Genet *47*, 615–624. https://doi.org/10.1038/ng.3293.

Morrissy, A.S., Garzia, L., Shih, D.J.H., Zuyderduyn, S., Huang, X., Skowron, P., Remke, M., Cavalli, F.M.G., Ramaswamy, V., Lindsay, P.E., et al. (2016). Divergent clonal selection dominates medulloblastoma at recurrence. Nature *529*, 351–357. https://doi.org/10.1038/nature16478.

Mulhern, R.K., Merchant, T.E., Gajjar, A., Reddick, W.E., and Kun, L.E. (2004). Late neurocognitive sequelae in survivors of brain tumours in childhood. The Lancet Oncology *5*, 399–408. https://doi.org/10.1016/S1470-2045(04)01507-4.

Nichol, J.A., and Hutter, O.F. (1996). Tensile strength and dilatational elasticity of giant sarcolemmal vesicles shed from rabbit muscle. J Physiol *493*, 187–198. .

Northcott, P.A., Shih, D.J.H., Peacock, J., Garzia, L., Sorana Morrissy, A., Zichner, T., Stütz, A.M., Korshunov, A., Reimand, J., Schumacher, S.E., et al. (2012a). Subgroup-specific structural variation across 1,000 medulloblastoma genomes. Nature *488*, 49–56. https://doi.org/10.1038/nature11327.

Northcott, P.A., Shih, D.J.H., Peacock, J., Garzia, L., Sorana Morrissy, A., Zichner, T., Stütz, A.M., Korshunov, A., Reimand, J., Schumacher, S.E., et al. (2012b). Subgroup-specific structural variation across 1,000 medulloblastoma genomes. Nature *488*, 49–56. https://doi.org/10.1038/nature11327.

Northcott, P.A., Buchhalter, I., Morrissy, A.S., Hovestadt, V., Weischenfeldt, J., Ehrenberger, T., Gröbner, S., Segura-Wang, M., Zichner, T., Rudneva, V.A., et al. (2017). The whole-genome landscape of medulloblastoma subtypes. Nature *547*, 311–317. https://doi.org/10.1038/nature22973.

Ocasio, J., Babcock, B., Malawsky, D., Weir, S.J., Loo, L., Simon, J.M., Zylka, M.J., Hwang, D., Dismuke, T., Sokolsky, M., et al. (2019). scRNA-seq in medulloblastoma shows cellular heterogeneity and lineage expansion support resistance to SHH inhibitor therapy. Nat Commun *10*, 5829. https://doi.org/10.1038/s41467-019-13657-6.

Ostrom, Q.T., Cioffi, G., Waite, K., Kruchko, C., and Barnholtz-Sloan, J.S. (2021). CBTRUS Statistical Report: Primary Brain and Other Central Nervous System Tumors Diagnosed in the United States in 2014–2018. Neuro-Oncology *23*, iii1–iii105. https://doi.org/10.1093/neuonc/noab200.

Pardo, L.A., and Stühmer, W. (2014). The roles of K+ channels in cancer. Nat Rev Cancer *14*, 39–48. https://doi.org/10.1038/nrc3635.

Pietuch, A., and Janshoff, A. (2013). Mechanics of spreading cells probed by atomic force microscopy. Open Biology *3*, 130084. https://doi.org/10.1098/rsob.130084.

Pietuch, A., Brückner, B.R., and Janshoff, A. (2013). Membrane tension homeostasis of epithelial cells through surface area regulation in response to osmotic stress. Biochimica et Biophysica Acta (BBA) - Molecular Cell Research *1833*, 712–722. https://doi.org/10.1016/j.bbamcr.2012.11.006.

Pollard, S.M., Yoshikawa, K., Clarke, I.D., Danovi, D., Stricker, S., Russell, R., Bayani, J., Head, R., Lee, M., Bernstein, M., et al. (2009). Glioma Stem Cell Lines Expanded in Adherent Culture Have Tumor-Specific Phenotypes and Are Suitable for Chemical and Genetic Screens. Cell Stem Cell *4*, 568–580. https://doi.org/10.1016/j.stem.2009.03.014.

R Core Team (2022). R: A Language and Environment for Statistical Computing (Vienna, Austria: R Foundation for Statistical Computing).

Rahrmann, E.P., Watson, A.L., Keng, V.W., Choi, K., Moriarity, B.S., Beckmann, D.A., Wolf, N.K., Sarver, A., Collins, M.H., Moertel, C.L., et al. (2013). Forward genetic screen for malignant peripheral nerve sheath tumor formation identifies new genes and pathways driving tumorigenesis. Nat Genet *45*, 756–766. https://doi.org/10.1038/ng.2641.

Raucher, D., and Sheetz, M.P. (1999). Membrane Expansion Increases Endocytosis Rate during Mitosis. Journal of Cell Biology *144*, 497–506. https://doi.org/10.1083/jcb.144.3.497.

Read, T.-A., Fogarty, M.P., Markant, S.L., McLendon, R.E., Wei, Z., Ellison, D.W., Febbo, P.G., and Wechsler-Reya, R.J. (2009). Identification of CD15 as a Marker for Tumor-Propagating Cells in a Mouse Model of Medulloblastoma. Cancer Cell *15*, 135–147. https://doi.org/10.1016/j.ccr.2008.12.016.

Riemondy, K.A., Venkataraman, S., Willard, N., Nellan, A., Sanford, B., Griesinger, A.M., Amani, V., Mitra, S., Hankinson, T.C., Handler, M.H., et al. (2021). Neoplastic and immune single-cell transcriptomics define subgroup-specific intra-tumoral heterogeneity of childhood medulloblastoma. Neuro-Oncology https://doi.org/10.1093/neuonc/noab135.

Rodal, S.K., Skretting, G., Garred, Ø., Vilhardt, F., van Deurs, B., and Sandvig, K. (1999). Extraction of Cholesterol with Methyl-β-Cyclodextrin Perturbs Formation of Clathrin-coated Endocytic Vesicles. Mol Biol Cell *10*, 961–974. .

Roffay, C., Molinard, G., Kim, K., Urbanska, M., Andrade, V., Barbarasa, V., Nowak, P., Mercier, V., García-Calvo, J., Matile, S., et al. (2021). Passive coupling of membrane tension and cell volume during active response of cells to osmosis. Proc Natl Acad Sci USA *118*, e2103228118. https://doi.org/10.1073/pnas.2103228118.

Sanguinetti, M.C., and Tristani-Firouzi, M. (2006). hERG potassium channels and cardiac arrhythmia. Nature *440*, 463–469. https://doi.org/10.1038/nature04710.

Schachter, N.F., Adams, J.R., Skowron, P., Kozma, Katelyn.J., Lee, C.A., Raghuram, N., Yang, J., Loch, A.J., Wang, W., Kucharczuk, A., et al. (2021). Single allele loss-of-function mutations select and sculpt conditional cooperative networks in breast cancer. Nat Commun *12*, 5238. https://doi.org/10.1038/s41467-021-25467-w.

Schüller, U., Heine, V.M., Mao, J., Kho, A.T., Dillon, A.K., Han, Y.-G., Huillard, E., Sun, T., Ligon, A.H., Qian, Y., et al. (2008). Acquisition of Granule Neuron Precursor Identity Is a Critical Determinant of Progenitor Cell Competence to Form Shh-Induced Medulloblastoma. Cancer Cell *14*, 123–134. https://doi.org/10.1016/j.ccr.2008.07.005.

Selvadurai, H.J., Luis, E., Desai, K., Lan, X., Vladoiu, M.C., Whitley, O., Galvin, C., Vanner, R.J., Lee, L., Whetstone, H., et al. (2020). Medulloblastoma Arises from the Persistence of a Rare and Transient Sox2+ Granule Neuron Precursor. Cell Reports *31*, 107511. https://doi.org/10.1016/j.celrep.2020.03.075.

Sigismund, S., Lanzetti, L., Scita, G., and Di Fiore, P.P. (2021). Endocytosis in the context-dependent regulation of individual and collective cell properties. Nat Rev Mol Cell Biol *22*, 625–643. https://doi.org/10.1038/s41580-021-00375-5.

Sitarska, E., and Diz-Muñoz, A. (2020). Pay attention to membrane tension: Mechanobiology of the cell surface. Current Opinion in Cell Biology *66*, 11–18. https://doi.org/10.1016/j.ceb.2020.04.001.

Speca, D.J., Ogata, G., Mandikian, D., Bishop, H.I., Wiler, S.W., Eum, K., Wenzel, H.J., Doisy, E.T., Matt, L., Campi, K.L., et al. (2014). Deletion of the Kv2.1 delayed rectifier potassium channel leads to neuronal and behavioral hyperexcitability. Genes, Brain and Behavior *13*, 394–408. https://doi.org/10.1111/gbb.12120.

Starr, T.K., Allaei, R., Silverstein, K.A.T., Staggs, R.A., Sarver, A.L., Bergemann, T.L., Gupta, M., O'Sullivan, M.G., Matise, I., Dupuy, A.J., et al. (2009). A transposon-based genetic screen in mice identifies genes altered in colorectal cancer. Science *323*, 1747–1750. https://doi.org/10.1126/science.1163040.

Starr, T.K., Scott, P.M., Marsh, B.M., Zhao, L., Than, B.L.N., O'Sullivan, M.G., Sarver, A.L., Dupuy, A.J., Largaespada, D.A., and Cormier, R.T. (2011). A Sleeping Beauty transposon-mediated screen identifies murine susceptibility genes for adenomatous polyposis coli (Apc)-dependent intestinal tumorigenesis. Proceedings of the National Academy of Sciences *108*, 5765–5770. https://doi.org/10.1073/pnas.1018012108.

Taylor, M.D., Northcott, P.A., Korshunov, A., Remke, M., Cho, Y.-J., Clifford, S.C., Eberhart, C.G., Parsons, D.W., Rutkowski, S., Gajjar, A., et al. (2012). Molecular subgroups of medulloblastoma: the current consensus. Acta Neuropathol *123*, 465–472. https://doi.org/10.1007/s00401-011-0922-z.

Temiz, N.A., Moriarity, B.S., Wolf, N.K., Riordan, J.D., Dupuy, A.J., Largaespada, D.A., and Sarver, A.L. (2016). RNA sequencing of *Sleeping Beauty* transposon-induced tumors detects transposon-RNA fusions in forward genetic cancer screens. Genome Res. *26*, 119–129. https://doi.org/10.1101/gr.188649.114.

Therneau, T.M., and Grambsch, P.M. (2000). Modeling survival data: extending the Cox model (New York: Springer).

Thottacherry, J.J., Kosmalska, A.J., Kumar, A., Vishen, A.S., Elosegui-Artola, A., Pradhan, S., Sharma, S., Singh, P.P., Guadamillas, M.C., Chaudhary, N., et al. (2018). Mechanochemical feedback control of dynamin independent endocytosis modulates membrane tension in adherent cells. Nature Communications *9*, 4217. https://doi.org/10.1038/s41467-018-06738-5.

Torkamani, A., Bersell, K., Jorge, B.S., Bjork, R.L., Friedman, J.R., Bloss, C.S., Cohen, J., Gupta, S., Naidu, S., Vanoye, C.G., et al. (2014). De novo KCNB1 mutations in epileptic encephalopathy. Ann Neurol *76*, 529–540. https://doi.org/10.1002/ana.24263.

Tronche, F., Kellendonk, C., Kretz, O., Gass, P., Anlag, K., Orban, P.C., Bock, R., Klein, R., and Schütz, G. (1999). Disruption of the glucocorticoid receptor gene in the nervous system results in reduced anxiety. Nat Genet *23*, 99–103. https://doi.org/10.1038/12703.

Uren, A.G., Mikkers, H., Kool, J., van der Weyden, L., Lund, A.H., Wilson, C.H., Rance, R., Jonkers, J., van Lohuizen, M., Berns, A., et al. (2009). A high-throughput splinkerette-PCR method for the isolation and sequencing of retroviral insertion sites. Nat Protoc *4*, 789–798. https://doi.org/10.1038/nprot.2009.64.

Vanner, R.J., Remke, M., Gallo, M., Selvadurai, H.J., Coutinho, F., Lee, L., Kushida, M., Head, R., Morrissy, S., Zhu, X., et al. (2014). Quiescent Sox2+ Cells Drive Hierarchical Growth and Relapse in Sonic Hedgehog Subgroup Medulloblastoma. Cancer Cell *26*, 33–47. https://doi.org/10.1016/j.ccr.2014.05.005.

Vladoiu, M.C., El-Hamamy, I., Donovan, L.K., Farooq, H., Holgado, B.L., Sundaravadanam, Y., Ramaswamy, V., Hendrikse, L.D., Kumar, S., Mack, S.C., et al. (2019). Childhood cerebellar tumours mirror conserved fetal transcriptional programs. Nature *572*, 67–73. https://doi.org/10.1038/s41586-019-1158-7.

Vodnala, S.K., Eil, R., Kishton, R.J., Sukumar, M., Yamamoto, T.N., Ha, N.-H., Lee, P.-H., Shin, M., Patel, S.J., Yu, Z., et al. (2019). T cell stemness and dysfunction in tumors are triggered by a common mechanism. Science *363*, eaau0135. https://doi.org/10.1126/science.aau0135.

Wang, X., Liu, H., Zhu, M., Cao, C., Xu, Z., Tsatskis, Y., Lau, K., Kuok, C., Filleter, T., McNeill, H., et al. (2018). Mechanical stability of the cell nucleus – roles played by the cytoskeleton in nuclear deformation and strain recovery. J Cell Sci *131*, jcs209627. https://doi.org/10.1242/jcs.209627.

Ward, R.J., Lee, L., Graham, K., Satkunendran, T., Yoshikawa, K., Ling, E., Harper, L., Austin, R., Nieuwenhuis, E., Clarke, I.D., et al. (2009). Multipotent CD15+ Cancer Stem Cells in Patched-1-Deficient Mouse Medulloblastoma. Cancer Research *69*, 4682–4690. https://doi.org/10.1158/0008-5472.CAN-09-0342.

Welf, E.S., Miles, C.E., Huh, J., Sapoznik, E., Chi, J., Driscoll, M.K., Isogai, T., Noh, J., Weems, A.D., Pohlkamp, T., et al. (2020). Actin-Membrane Release Initiates Cell Protrusions. Developmental Cell *55*, 723-736.e8. https://doi.org/10.1016/j.devcel.2020.11.024.

Wu, X., Northcott, P.A., Dubuc, A., Dupuy, A.J., Shih, D.J.H., Witt, H., Croul, S., Bouffet, E., Fults, D.W., Eberhart, C.G., et al. (2012). Clonal selection drives genetic divergence of metastatic medulloblastoma. Nature *482*, 529–533. https://doi.org/10.1038/nature10825.

Yang, Z.-J., Ellis, T., Markant, S.L., Read, T.-A., Kessler, J.D., Bourboulas, M., Schüller, U., Machold, R., Fishell, G., Rowitch, D.H., et al. (2008). Medulloblastoma Can Be Initiated by Deletion of Patched in Lineage-Restricted Progenitors or Stem Cells. Cancer Cell *14*, 135–145. https://doi.org/10.1016/j.ccr.2008.07.003.

Zhang, L., He, X., Liu, X., Zhang, F., Huang, L.F., Potter, A.S., Xu, L., Zhou, W., Zheng, T., Luo, Z., et al. (2019). Single-Cell Transcriptomics in Medulloblastoma Reveals Tumor-Initiating Progenitors and Oncogenic Cascades during Tumorigenesis and Relapse. Cancer Cell S1535610819303368. https://doi.org/10.1016/j.ccell.2019.07.009.

(2003). Manipulating the mouse embryo: a laboratory manual (Cold Spring Harbor, N.Y: Cold Spring Harbor Laboratory Press).

FIGURE LEGENDS

Figure 1. The Lazy Piggy transposon system enriches for cancer maintenance drivers

(A) Cartoon illustrating the rationale and design of the Lazy Piggy (LP) transposon system. Tumors harbor myriad mutations and genetic alterations, which can be classified as drivers and passengers (garbage). Drivers encompass initiation (match), maintenance (wood), and progression (gasoline) events. Initiating drivers transform non-tumor cells of origin to initiate tumorigenesis, maintenance drivers sustain continued tumor growth, and progression drivers elevate the malignant or metastatic potential of the tumor. Only targeting maintenance drivers will cause clonal collapse and tumor regression.

(B) First, Sleeping Beauty (SB)-induced insertional mutagenesis drives MB progression. Second, low-dose tamoxifen induces PB-mediated remobilization, restoring original gene function of select insertion events.

(C) While insertions at initiator, passenger, and progression genes are depleted with no consequence on tumor survival, transposon remobilization from maintenance drivers results in clonal collapse and depletion. Thus, this strategy enriches for retention of insertions at maintenance drives.

Figure 2. Lazy Piggy screening implicates potassium channels in medulloblastoma maintenance

(A) *Ptch1*$^{+/-}$ mice with LP transposition experienced poorer survival compared to *Ptch1*$^{+/-}$ mice or mice with LP transposition alone.

(B) Overview of the significant gCIS insertions in candidate genes from all sequenced samples (n = 62) comprised of tamoxifen-negative tumors with 'parental insertions' that have not been remobilized, and tamoxifen-treated tumors with maintenance 'driver insertions' enriched by piggyBac-mediated transposon remobilization.

(C) RNA-seq differential expression of tamoxifen-treated versus untreated tumors. Pink dots represent genes upregulated in tamoxifen-treated tumors that have been enriched for maintenance insertions. Outlier gene *Scd2* omitted for visualization (log2FC 0.49; p_{adj} 1e-11).

(D-G) KCNB2 is upregulated among potassium channels in published data across human WNT (n = 56), SHH (n = 182), Group 3 (n = 131), and Group 4 medulloblastoma (n = 289) compared to human control cerebellum (n = 9) (Northcott et al., 2012b). Significantly differentially expressed genes are indicated in color (log_2fold change > 1, $P_{adj} < 0.05$).

(H) Potassium channel phylogeny (gray lines) illustrating potassium channel genes identified from the Lazy Piggy screen (blue lines) and the most over-expressed potassium channel from patient expression analysis (red line). Bolded text indicates different classes of potassium channel genes (K_v, K_{2P}, K_{CA}, K_{IR}, $K_V\beta$, KCNE, KChIP).

Figure 3. Kcnb2 is a medulloblastoma-specific vulnerability

(A) Kaplan-Meier survival plot of *Kcnb2*$^{+/+}$, *Kcnb2*$^{+/-}$, and *Kcnb2*$^{-/-}$ mice.

(B) Genotypes of offspring obtained from crossing *Kcnb2*$^{+/-}$ parents.

(C) Weight of *Kcnb2*$^{+/+}$, *Kcnb2*$^{+/-}$, and *Kcnb2*$^{-/-}$ mice at postnatal day 21.

(D) Litter sizes obtained from breeding pairs of *Kcnb2*$^{+/+}$, *Kcnb2*$^{+/-}$, and *Kcnb2*$^{-/-}$ mice.

(E) Representative histology of sagittal brain sections from P7 and P30 mice.

(F) Representative immunohistochemistry of Sox2, GFAP, and Calbindin from sagittal cerebellum sections of *Kcnb2*$^{+/+}$ and *Kcnb2*$^{-/-}$ mice.

(G) Kaplan-Meier survival plot *Math1-Cre; SmoM2* with *Kcnb2*$^{+/+}$, *Kcnb2*$^{+/-}$, *Kcnb2*$^{-/-}$ alleles.

(H) Representative images of P21 *Math1-Cre; SmoM2* and *Math1-Cre; SmoM2; Kcnb2*$^{-/-}$ mice displaying brain tumor-induced cranial bulging (left) and tumor burden (right).

(I) Expression and quantification of *Kcnb2*, *Sox2*, and *Dcx* in a *Math1-Cre; SmoM2* tumor detected by RNAscope single-molecule in situ hybridization.

(J-K) Nebulosa plot showing co-expression of *KCNB2* with *SOX2* and *DCX* in previously published human SHH MB single-cell RNA sequencing data (Hovestadt et al., 2019; Riemondy et al., 2021).

Figure 4. Kcnb2 regulates SHH MB-propagating cells

(A) Analysis of Sox2^{+} cells in P21 MBs with or without Kcnb2 knockout.

(B) Schematic of BrdU pulse experiment.

(C) Representative images of Sox2 and Ki67 immunohistochemistry from P7 MBs.

(D) Quantification of Ki67^{+} cycling proportion of Sox2^{+} MPCs at P7 and P21.

(E) Quantification of Sox2^{+} cell cycle retention at P7 and P21.

(F) Quantification of Sox2^{+} S-phase retention at P7.

(G) Representative images of Dcx and Ki67 immunohistochemistry from P7 MBs.

(H) Quantification of Ki67^{+} cycling proportion of Dcx^{+} MB cells at P7.

(I) Quantification of Dcx^{+} cell cycle retention at P7.

Figure 5. Kcnb2 regulates membrane tension of MB-propagating cells

(A) Top: Schematic for isolation and culture of Sox2^{+} MPCs. Bottom: 6-day cell counting assay comparing control and Kcnb2 knockout MPCs.

(B) Primary and secondary *in vitro* sphere-forming limiting dilution analysis (LDA) comparing control and Kcnb2-knockout MPCs, and control MPCs treated with 2.5 mM 4-Aminopyridine (4-AP).

(C) Representative current traces show total currents from whole-cell recordings of Sox2^{+} MPCs. Currents are elicited by voltage steps from -80 mV to 80 mV in 20-mV increments.

(D) Current-voltage (I-V) curves of control and Kcnb2 knockout MPCs.

(E) Cell capacitance of control and Kcnb2 knockout MPCs.

(F) 3D-reconstruction and quantification of Sox2^{+} MPC volume as measured by SmoM2-YFP signal.

(G) Schematic illustrating membrane tension, inner cell pressure, and membrane tethering.

(H) Apparent membrane tension analysis of control and Kcnb2 knockout MPCs. (Top) Schematic and images shown for the probes used for atomic force microscopy experiments.

(I) Inner cell pressure analysis of control and Kcnb2 knockout MPCs. (Top) Schematic and images show micropipette aspiration technique used.

(J) Representative images of Sox2$^+$ MPCs treated with 2.5 mM 4-aminopyridine (4-AP) and 5 mM tetraethylammonium (TEA).

(K) Quantification of Sox2$^+$ MPC volume as measured by α-Tubulin signal treated with 2.5 mM 4-aminopyridine (4-AP) and 5 mM tetraethylammonium (TEA).

(L) Apparent membrane tension of Sox2$^+$ MPCs treated with 2.5 mM 4-aminopyridine (4-AP) and 5 mM tetraethylammonium (TEA).

Figure 6. Kcnb2 regulates endocytosis of EGFR in MB-propagating cells

(A) Experimental schematics for manipulating osmolarity to assess membrane tethering.

(B) Analysis of pERM membrane tethering and cell size in control and Kcnb2 knockout MPCs under hypertonic, isotonic, and hypotonic conditions. Quantifications show co-localized pERM$^+$; F-actin$^+$ signal normalized to total F-actin$^+$ volume (left) and cell size as assessed by SmoM2-YFP volume (right). Hypertonic conditions were achieved by addition of 3.75% polyethylene glycol (PEG) 1500 for 24 hrs. Hypotonic conditions were achieved by addition of 30% de-ionized water for 24 hrs.

(C) Representative immunocytochemistry for pERM and F-actin in wild-type and Kcnb2 knockout MPCs under hypertonic, isotonic, and hypertonic conditions.

(D) Schematic representation of cell size and biomechanical changes upon Kcnb2 knockout.

(E) Representative images of endocytic markers Caveolin-1, Clathrin, and Rab5 in Sox2$^+$ MPCs.

(F) Representative images of phosphorylated EGFR (pEGFR) signal in Sox2$^+$ MPCs.

(G) Quantification of Caveolin-1, Clathrin, Rab5 puncta, and pEGFR signal in Sox2$^+$ MPCs.

(H) Representative images and quantification of pEGFR$^+$ and Caveolin-1$^+$ colocalization in Sox2$^+$ MPCs.

(I) Total internal reflection fluorescence (TIRF) microscopy and quantification of the membrane fraction of Caveolin-1 and pEGFR in Sox2$^+$ MPCs.

Figure 7. Ionic control of membrane tension and EGFR potentiate MB cell proliferation

(A-B) Representative immunohistochemistry (A) and quantification (B) of Sox2, pERM, Caveolin-1, and pEGFR, in P7 control and Kcnb2 knockout *Math1-Cre; SmoM2* MB.

(C) Schematic of experiments to manipulate membrane tension. (Left) Control Sox2$^+$ MPCs are treated with NSC668394, an inhibitor of ezrin phosphorylation, to reduce membrane tension. (Right) Kcnb2 knockout Sox2$^+$ MPCs are treated with Methyl-β-cyclodextrin (MβCD), which depletes cholesterol from plasma membrane to increase membrane tension.

(D) Quantification of SmoM2$^+$ cell volume, Caveolin-1$^+$ puncta, and pEGFR$^+$ signal in control Sox2$^+$ MPCs treated with 25 μM NSC668394 (NSC) for 24 hrs *in vitro*.

(E) Quantification of SmoM2$^+$ cell volume, Caveolin-1$^+$ puncta, and pEGFR$^+$ signal in Kcnb2 knockout Sox2$^+$ MPCs treated with 1 mM MβCD for 24 hrs *in vitro*.

(F) BrdU incorporation in Sox2$^+$ MPCs after incubating for 3 hours. Results are expressed as fold change relative to control MPCs in standard culture conditions with 10 ng/mL EGF.

(G) (Left) Schematic of vismodegib treatment regimen. (Right) Control and Kcnb2 knockout MB-bearing mice were treated on three consecutive days with vismodegib or vehicle and monitored for survival.
(H) Physiological and molecular mechanism of action for Kcnb2 in MB.

Supplemental figure 1. Generation and validation of transgenic mice harboring Lazy Piggy transposon
(A) PCR amplification of LP concatemer region in transfected 293T cells. Combinations performed in triplicate with 50ng, 100ng, and 150ng input DNA each.
(B) Immunofluorescence of 293T cells transfected with LP transposon and PB-ER transposase demonstrated nuclear localization of PB transposase following tamoxifen administration.
(C) Microinjection of 4-unit concatemer of the LP transposon generated 7 founder mice.
(D) qPCR determination of LP concatemer copy number in founder mice.
(E) Western blot analysis of cerebellar ERα expression in *R26-LSL-PB-ER*$^{T2+/-}$ mice when crossed with *Nestin-Cre*$^{+/-}$ mice.
(F) PCR amplification of LP concatemer region demonstrates SB and PB mobilization with tamoxifen treatment in *Ptch1*$^{+/-}$*; Nestin:Luc-SB100*$^{+/-}$*; Lazy Piggy*$^{+/-}$*; Nestin-Cre*$^{+/-}$*; R26-LSL-PB-ER*$^{T2+/-}$ mice. Combinations performed in triplicate with 50ng, 100ng, and 150ng input DNA each.
(G) Tamoxifen treatment was not associated with overall survival in *Ptch1*$^{+/-}$*; Nestin:Luc-SB100*$^{+/-}$*; Lazy Piggy*$^{+/-}$*; Nestin-Cre*$^{+/-}$*; R26-LSL-PB-ER*$^{T2+/-}$ mice.
(H) Tumors in *Ptch1*$^{+/-}$*; Nestin:Luc-SB100*$^{+/-}$*; Lazy Piggy*$^{+/-}$*; Nestin-Cre*$^{+/-}$*; R26-LSL-PB-ER*$^{T2+/-}$ mice histologically resembled human medulloblastoma (H&E staining).

Supplemental figure 2. Detection and analysis of Lazy Piggy transposon remobilization
(A) Cartoon illustrating library preparation workflows for SB Inverted Repeat (IR), piggyBac (PB), and Excision Junction (JX) libraries.
(B) Heatmap of Jaccard score similarity matrix for clonal IR and JX library insertions in sequenced mouse tumors.
(C) Tamoxifen-treated tumors show a higher proportion of IR/JX overlap than untreated tumors.
(D) Map of all sequenced insertions annotated to *Kcnb1* suggests gain-of-function given biases toward intronic, 5', and sense-oriented insertions.
(E) Map of all sequenced insertions annotated to *Kcnh2* suggests loss-of-function given the span of insertions across the entire coding sequence of *Kcnh2* which would yield a truncated and non-functional channel.
(F) Dimensionality reduction by uniform manifold approximation and projection (UMAP) of DESeq2-normalized RNA-seq counts from tamoxifen-treated and untreated tumors.

Supplemental figure 3. Analysis of Kcnb2 function in mouse cerebellar development
(A) Representative images P21 *Kcnb2*$^{+/+}$, *Kcnb2*$^{+/-}$, and *Kcnb2*$^{-/-}$ littermate mice.
(B) Representative images of P7 and P30 brains of *Kcnb2*$^{+/+}$ and *Kcnb2*$^{-/-}$ mice.

(C) Quantification of molecular layer, internal granule layer, external granule layer thickness, Calbindin$^+$ Purkinje neuron and Sox2$^+$ Bergmann glia populations of P7 *Kcnb2*$^{+/+}$ and *Kcnb2*$^{-/-}$ mice.

(D) Quantification of molecular layer, internal granule layer thickness, Calbindin$^+$ Purkinje neuron and Sox2$^+$ Bergmann glia populations of P30 *Kcnb2*$^{+/+}$ and *Kcnb2*$^{-/-}$ mice.

(E) Representative immunohistochemistry images from cerebella of P7 *Kcnb2*$^{+/+}$ and *Kcnb2*$^{-/-}$ mice.

(F) Representative immunohistochemistry images from cerebella of P30 *Kcnb2*$^{+/+}$ and *Kcnb2*$^{-/-}$ mice.

Supplemental figure 4. Phenotypic analysis of control and Kcnb2 knockout MB

(A-B) Quantification of Sox2$^+$ cells in MB of P7 *Math1-Cre; SmoM2* mice with and without Kcnb2.

(C-D) Quantification of phosphor-Histone 3$^+$ (pHis3$^+$) cells in MB of P7 *Math1-Cre; SmoM2* mice with and without Kcnb2.

(E) Representative immunohistochemistry of TUNEL$^+$ puncta and Sox2$^+$ cells in MB of P21 *Math1-Cre; SmoM2* mice with and without Kcnb2.

(F) Quantification of TUNEL$^+$; Sox2$^+$ cells in P7 and P21 MB of *Math1-Cre; SmoM2* mice with and without Kcnb2.

(G) Quantification of TUNEL$^+$ tumor cells in P21 MB of *Math1-Cre; SmoM2* mice with and without Kcnb2.

Supplemental figure 5. BrdU label retention analysis of MB

(A) Experimental design of BrdU label retention analysis. *Math1-Cre; SmoM2* and *Math1-Cre; SmoM2; Kcnb2*$^{-/-}$ mice were injected with a single dose of BrdU and sacrificed at the indicated timepoints (n = 3-4 mice per group).

(B) Representative images of BrdU label retention in Sox2$^+$, Dcx$^+$, and NeuN$^+$ cells at 1, 3, and 7 days after BrdU injection in MB of *Math1-Cre; SmoM2* mice.

(C-F) Percentage of BrdU retention in all tumor cells (C), Sox2$^+$ cells (D), Dcx$^+$ cells (E), and NeuN$^+$ cells (F).

Supplemental figure 6. Ligand titration assay and western blot in Sox2$^+$ MPCs *in vitro.*

(A) Sox2$^+$ MPCs were cultured in media with indicated concentrations of EGF and bFGF and assessed for relative viability by MTS assay (left) and crystal violet staining (right).

(B) Western blot and quantification of four pairs of control and Kcnb2 knockout MPCs for pEGFR, EGFR, pERM, Ezrin, and Coomassie blue dye. All quantifications were normalized to the total Coomassie blue signal per lane.

METHODS

Lazy Piggy plasmid construction

The Lazy Piggy transposon was custom synthesized and is shown in Figure 1B. Mammalian-optimized PB minimum ITRs, as previously published (Cadiñanos and Bradley, 2007), were introduced to the T2/Onc2 SB transposon, nested between SB ITRs. T2/Onc2, as previously published (Dupuy et al., 2005), contained a murine stem cell virus long terminal repeat (MSCV) 5' LTR, a splice donor (SD) from exon 1 of the mouse Foxf2 gene, one splice acceptor (SA) from exon 2 of the mouse engrailed-2 (En2) gene and another from the carp β-actin gene, followed by a bidirectional SV40 poly(A) sequence. Restriction sites AcII and ClaI were introduced flanking the transposon sequence and a 4-copy concatemer was cloned into the pUC19 vector, hence termed "pLazyPiggy." Detailed cloning methods available upon request.

In vitro validation of the Lazy Piggy system

HEK293T cells were cultured in DMEM (GIBCO) supplemented with 10% fetal bovine serum at 37°C and 5% CO_2. 5×10^5 cells were seeded into each well of a 6-well plate 1 day prior to transfection. For each well, 2μg circular plasmids pCMV-HA-mPB-ERT2 (Cadiñanos and Bradley, 2007), pLazyPiggy, and pCMV-SB11 (Wu et al., 2012) were transfected using Lipofectamine LTX as per manufacturer's protocol (Invitrogen). Cells were then incubated with 2 μM 4-hydroxytamoxifen (4-OHT) for 24 hours. Cells were then collected and gDNA were extracted for PCR excision assays. Primers for amplifying LP-transposon mobilization were based on the cloning vector sequences adjacent to the inverted repeats/direct repeats (left) (IRDRL) and inverted repeats/direct repeats (right) (IRDRR) of the LP transposon, 5'-CGTTCACGACGTTGTAAAACGACG-3' and 5'-CGATAATTAACCCTCACTAAAGGG-3', respectively. The input represents genomic DNA with LP intact transposon (2791bp), post-SB mobilization (166bp) and post-PB re-mobilization (681bp) in the presence of 4-OHT. Detailed PCR protocol methods are available upon request.

Novel mouse line generation

Nestin-Cre transgenic mice obtained from Jackson Laboratories (JAX stock #003771). To generate *Nestin:Luc-SB100* transgenic mice, SB100 cDNA was excised from the vector pCMV-SB100 (Mátés et al., 2009), luciferase-tagged, then inserted into nes1852tk/lacZ plasmid, which carried the Nestin second intronic enhancer that has previously been shown to drive transgene expression in CNS stem and progenitor cells (Kawaguchi et al., 2001). *Rosa26-LSL-mPB-L3-ERT2* transgenic mice were obtained from Dr. Allan Bradley (Li et al., 2013). Lazy Piggy transgenic mice were produced by pronuclear microinjection into zygotes by the Transgenic Core at The Centre for Phenogenomics (TCP) (2003). High-percentage male chimeras were crossed to C57/BL6 females. Germline transmission was confirmed by genotyping F1 offspring tail-clipped DNA. Primers used were: LP Fwd 5'-CGATAAAACACATGCGTC -3', LP Rev 5'- CTCCAAGCGGCGACTGAG -3'.

Lazy Piggy founder copy number was determined through qPCR as previously described (Joshi et al., 2008). Briefly, a linear equation was modelled of C_T values against copy number from 9 known LP transposon plasmid

standards in triplicate, then C_T values from triplicate founder samples were input to this model and resulting predicted copy numbers were averaged. Two founders (#129 and #137) were chosen for having “high” and “medium” LP copy numbers, respectively, on separate donor chromosomes.

Western blot analysis

Western blot analysis was performed on postnatal day 30 cerebellum from transgenic mice *R26:LSL-PB-ERT2*$^{+/-}$ mice crossed with *Nestin-Cre*$^{+/-}$ mice. Extracted protein was run on Novex Wedgewell 8–16% Tris-Glycine gradient gels (Thermo Fisher) then transferred to PVDF membranes. Membranes were then blocked in TTBS with 5% Skim milk (Bioshop #SKI400) for two hours and probed overnight in TTBS/1% skim milk with a 1:3000 dilution of mouse anti-α-Tubulin (Sigma Aldrich #T6199), or a 1:500 dilution of mouse anti-Erα antibody (SCBT sc-56833). Membranes were then washed in TTBS/1% skim milk, incubated with secondary antibodies (1:5000 anti-mouse IgG, HRP-linked antibody (Cell Signaling #7076S)). Finally, blots were washed in TTBS/1% skim milk, incubated in Pierce ECL Western substrate (Thermo Fisher #32209) and signal visualized on a Bio-Rad ChemiDoc system.

Necropsy, tumor collection, and histological analysis

Experimental mice were monitored for tumor formation over a period of 365 days. When mice reached humane endpoint, they were sacrificed according to Canadian Council on Animal Care (CACC) guidelines. Upon sacrifice, cerebellar tumors were collected and divided into smaller pieces and frozen on dry ice. Samples were placed at −80 °C for long-term storage or in RNAlater (Sigma). Formalin-fixed tissue samples were paraffin-embedded by the Pathology Core at the Centre for Modeling Human Disease (CMHD) in TCP. 5 µm sections were stained with Hematoxylin and Eosin and used for histological analysis.

Histological analysis

Formalin-fixed tissue samples were paraffin-embedded by the Pathology Core at the Centre for Modeling Human Disease (CMHD) in TCP. 5 µm sections were stained with Hematoxylin and Eosin, and used for histological analysis.

Library preparation and sequencing

Restriction-splink PCR was performed based on previous protocols (Largaespada and Collier, 2008; Uren et al., 2009). In brief, mouse tumour gDNA was extracted and mechanically sheared to 300 bp fragments using a Covaris S220 sonicator. End repair was then performed using a EpiCentre End-It Kit, followed by adaptor ligation. With splinkerette-adaptors ligated at both ends, BamHI was used to digest and remove gDNA fragments. Primary and secondary PCR amplifications were performed using primers listed below for Left & Right amplification and for barcoding, respectively. Finally, purified PCR products were sent for 454 parallel sequencing at the Ontario Institute for Cancer Research. Genomic DNA libraries from LP tumours were prepared as sequenced as previously described (Schachter et al., 2021). Three libraries were prepared to identify different types of LP

insertion events. To identify all LP insertions, LP insertions that had undergone PB excision, and LP insertions that had not undergone PB excision, the IR, PB, and JX libraries were prepared using primers corresponding to individual SB ITRs, both SB ITRs, and SB plus PB ITRs, respectively.

Primers to generate adaptors:

Linker+: 5'-GTAATACGACTCACTATAGGGCTCCGCTTAAGGGAC-3'

Linker-: 5'-Phos-GTCCCTTAAGCGGAG-C3spacer-3'

Primary PCR primers for Left and Right amplification:

IRL (left): 5'-AAATTTGTGGAGTAGTTGAAAAACGA-3'

IRR (right): 5'-GGATTAAATGTCAGGAATTGTGAAAA-3'

Linker-A1 primer: 5'-GTAATACGACTCACTATAGGGC-3'

Secondary PCR primers for barcoding:

IR-barcoded primer:

5'-AATGATACGGCGACCACCGAGATCTACACTCTTTCCCTACACGACGCTCTTCCGATCT(barcode)TGTATGTAAACTTCCGACTTCAACTG-3'

LinkerA2_PE (for paired-end sequencing):

5'-CAAGCAGAAGACGGCATACGAGATCGGTCTCGGCATTCCTGCTGAACCGCTCTTCCGATCTTAGGGCTCCGCTTAAGGGAC-3'

Primary PCR primers:

PBL (left): 5'-CGATAAAACACATGCGTC-3'

PBR (right): 5'-CTCCAAGCGGCGACTGAG-3'

PBL2 (left): 5'-AAACCTCGATATACAGACCGAT-3'

PBR2 (right): 5'-TTACCGCATTGACAAGCACGCC-3'

Linker-A1: 5'-GTAATACGACTCACTATAGGGC-3'

Secondary PCR primers (17 bp shared in both directions):

PB-barcoded primer: 5'-AATGATACGGCGACCACCGAGATCTACACTCTTTCCCTACACGACGCTCTTCCGATCT(barcode)tatctttctaggttaa-3'

PB-barcoded P1: 5'-AATGATACGGCGACCACCGAGATCTACACTCTTTCCCTACACGACGCTCTTCCGATCTAAGAAGAAtatctttctagggttaa-3'

PB-barcoded P2: 5'-AATGATACGGCGACCACCGAGATCTACACTCTTTCCCTACACGACGCTCTTCCGATCTGGCAAGAAtatctttctagggttaa-3'

PB-barcoded P3: 5'-AATGATACGGCGACCACCGAGATCTACACTCTTTCCCTACACGACGCTCTTCCGATCTCCTAAGAAtatctttctagggttaa-3'

PB-barcoded P4: 5'-AATGATACGGCGACCACCGAGATCTACACTCTTTCCCTACACGACGCTCTTCCGATCTCGAGAGAAtatctttctagggttaa-3'

LinkerA2_PE (for paired end sequencing):

5'-CAAGCAGAAGACGGCATACGAGATCGGTCTCGGCATTCCTGCTGAACCGCTCTTCCGATCTTAGGGCTCCGCTTAAGGGAC-3'

<u>Primary and secondary Sleeping Beauty PCR primers:</u>

<u>Junction PCR:</u>

PBLJ	5'-gtagcattgcagtactaagc-3'
PBLJ2	5'-gtatttggtagcattgcagt-3'
PBRJ	5'-cactaagttgagtactaagc-3'
PBRJ2	5'-ggtcagaagtttacatacac-3'
PBLJX (Overlap)	5'-gcttttaaattgttaagcacaagc-3'
PBLJX2 (Overlap)	5'-ctaagcttttaaattgttaagcacaagc-3'
PBRJX (Overlap)	5'-actaagcttgtgcttaacaatt-3'
PBRJX2 (Overlap)	5'-gttgagtactaagcttgtgcttaacaat-3'
PBLJ3	5'-gcattgcagtactaagcttttaaat-3'
PBLJ4	5'-tggtagcattgcagtactaagctt-3'
PBLJ5	5'-ctcaattagtatttggtagcattgcag-3'
PBRJ3	5'-cactaagttgagtactaagcttgtg-3'
PBRJ4	5'-catacactaagttgagtactaagcttg-3'
PBRJ5	5'-gtcagaagtttacatacactaagttgag-3'

LP read processing, alignment and analysis

Processing and gCIS analysis of Lazy Piggy transposon insertion sites were performed using a custom R script. To correct for technical alignment jitter in insertion mapping, insertions were grouped by sample and orientation (left or right), then counts were aggregated for insertions within 5bp of each other. We removed insertions mapping to non-standard or donor chromosomes, those with single read support, or those detected in *Ptch1*$^{+/-}$ control mice. A dynamic filter was used to categorize insertions as clonal or subclonal, as previously described (Brett et al., 2011; Schachter et al., 2021). For each library, three thresholds were calculated using the insertion data: (i) >95th percentile of reads under the negative binomial distribution fit to the number of sites with 1–3 reads, (ii) 1% of the read count of the most abundant insertion site, (iii) 0.1% of the total read number. The most stringent value was the threshold for clonal insertions and the second-most was the threshold for the clonal/subclonal category. Gene-centric common insertion site (gCIS) analysis was performed using clonal/subclonal insertions. gCIS genes were RefSeq genes (+15kb buffer) with insertions in at least 3 separate tumors and Bonferroni-corrected p value <0.05 from a Chi-square test of observed and expected insertion counts given the number of TA dinucleotide sites within the gene relative to the whole genome and the total number of insertions within each tumor. Known false positive genes *En2*, *Sfi1,* and *Foxf2* were removed since they contain sequence homology with the LP transposon. To identify tumor maintenance genes, we compared gCIS genes from PB libraries in mice with and without tamoxifen treatment. To assess robustness of tamoxifen-induced PB remobilization, Jaccard similarity scores were calculated for all pair-wise library comparisons in IR and JX libraries.

Bulk RNAseq library preparation, data preprocessing, and analysis (Lazy Piggy tumours)

Bulk RNAseq libraries were prepared and sequenced as previously described (Temiz et al., 2016) using the Miseq system with 5 samples pooled per lane and mean 50 million reads per sample. After raw FASTQ quality check with FastQC, reads were aligned using STAR (2.5.4b) to mouse genome mm9 using the annotation file Mus musculus NCBIM37v67 (downloaded from Ensembl) with masking for the *En2* gene, whose splice acceptor sequence is contained in the LP transposon (Dobin et al., 2013). The “ReadsPerGene” raw counts from STAR were used for differential expression analysis with DESeq2 (1.34.0) using genes with non-zero counts in at least two samples per tamoxifen treatment group (Love et al., 2014). Dimensionality reduction by UMAP (McInnes et al., 2020) was then performed to visualize the distribution of tamoxifen receipt status across clusters following variance-stabilizing transformation of raw counts in DESeq2.

Bulk RNAseq analysis (Human MB and normal cerebellum)

Normalized counts were generated from published human MB and normal cerebellar bulk RNAseq data as described previously (Northcott et al., 2012b, 2017; Vladoiu et al., 2019). DESeq2 (1.34.0) was used for differential expression analysis (Love et al., 2014).

Single cell RNAseq analysis

Normalized counts for human SHH MB samples were downloaded from GEO (Hovestadt et al., 2019) and UCSC Cell Browser (Riemondy et al., 2021) and prepared as Seurat (4.1.0) objects. UMAP embeddings for the data from Riemondy et al. were directly downloaded. UMAP embeddings for Hovestadt et al. were calculated following the Seurat SCTransform() vignette and batch effects corrected using {harmony} (0.1.0) with all default settings. Joint densities were plotted to visualize co-expression of selected genes using {Nebulosa} (1.4.0).

Mouse studies

All procedures were performed in compliance with the Animals for Research Act of Ontario and the Guidelines of the Canadian Council on Animal Care. The Centre for Phenogenomics (TCP) Animal Care Committee reviewed and approved our protocol 19-0288H. In all cases, mice were maintained on a 12-hour light/dark cycle with free access to food and water. For all studies, mice of either sex were used, and randomly allocated to experimental groups. *Ptch1*$^{+/-}$ (Goodrich et al., 1997), *Math1-Cre* (Matei et al., 2005), *Rosa26-LSL-SmoM2-YFP* (*SmoM2*) (Jeong et al., 2004), *Kcnb2*$^{-/-}$ (*Kcnb2*^{tm1Lex}) (Hermanstyne et al., 2010), and *Nestin-Cre* (Tronche et al., 1999) mice were previously described. All mice were bred and genotyped as recommended by Jackson Laboratories. *Math1-Cre; SmoM2* mice develop SHH MB due to expression of SmoM2—a constitutively active form of the SHH pathway receptor Smoothened—in cerebellar granule neuron precursors (CGNPs), achieved by CGNP-specific driver *Math1-Cre* (Schüller et al., 2008; Yang et al., 2008). *Ptch1*$^{+/-}$ mice develop SHH MB due to loss of one allele of the SHH pathway inhibitor *Ptch1* (Goodrich et al., 1997) and subsequent loss-of-heterozygosity, which drives constitutive SHH signaling in CGNPs.

For anti-Hedgehog therapy, 50 mg/kg vismodegib (GDC-0449, Selleck Chemical) was administered three times (P18, 19, 20) in 4.76% DMSO 0.5% methylcellulose 0.2% Tween 80 buffer by intraperitoneal injection. For single-dose BrdU labeling, mice were injected intraperitoneally with 50 mg/kg BrdU (Roche) in PBS. Tamoxifen-citrate mixture at 400 mg/kg was incorporated to the standard rodent diet premixed with ~5% sucrose as a palatability enhancer (Harlan Laboratories Teklad Diets). Tamoxifen chow was introduced once tumour-induced cranial bulge visualized, typically 45–60 days postnatal.

Mouse Sox2^{+} MB cell isolation and culture

Mouse Sox2^{+} MB cells were isolated as previously described (Huang et al., 2010). Briefly, brain tumors from P7 *Math1-Cre; SmoM2* mice were dissociated by repetitive pipetting using ice-cold PBS without Mg^{2+} and Ca^{2+}, followed by treatment using 50% Accutase (Stemcell Technologies) diluted in PBS. Dissociated cells were cultured on plates coated with poly-L-ornithine (Sigma-Aldrich) and laminin (Sigma-Aldrich), using Neurocult NS-A Basal media (StemCell Technologies) supplemented with 2 mM L-glutamine, N2, B27, 75 µg/ml BSA, 2 µg/ml Heparin, 10 ng/ml basic FGF and 10 ng/ml human EGF without addition of serum. All cell lines were regularly checked for mycoplasma infections.

For cell counting assays, cells were plated at a density of 2000 cells per well in poly-L-ornithine- and laminin-coated 12 well plates. At 2, 4, or 6 days after seeding, cells were resuspended using Accutase and incubated in isotonic solution. Cell count was acquired using a Multisizer 4 Coulter Counter (Beckman-Coulter) using standard protocols and a threshold of 12 to 30 µm.

Immunocytochemistry

Immunocytochemistry was performed on cultured cells as previously described (Chen et al., 2018). Briefly, cells on glass coverslips were fixed for 15 minutes with 4% PFA and then permeabilized with 0.1% Triton X-100 in PBS (PBST). Cells were subsequently blocked with 10% normal goat serum in PBST for one hour at room temperature and incubated with primary antibodies in blocking solution overnight at 4° C, followed by incubation with fluorophore-conjugated secondary antibodies (1:400-1000) and 1 µg/ml DAPI (Sigma-Aldrich) for one hour at room temperature. For F-actin staining, cells were stained with 1:500 Alexa Fluor 488 Phalloidin (Invitrogen). Coverslips were mounted onto glass slides using Prolong Gold (Invitrogen). The primary antibodies include: chicken anti-GFP (Antibodies Incorporated #GFP-1020, 1:1000), mouse anti-α-Tubulin (Sigma-Aldrich #T6199, 1:1000), mouse anti-BrdU (DSHB #G3G4, 1:1000), mouse anti-Caveolin-1 (Novus #NB100-615, 1:200), rabbit anti-Caveolin-1 (Cell Signaling Technology #3267, 1:400), rabbit anti-Clathrin Heavy Chain (Cell Signaling Technology #4796, 1:100), rabbit anti-pEGFR (Cell Signaling Technology #3777, 1:800), rabbit anti-pEGFR (abcam #ab40815, 1:250), rabbit anti-pERM (Cell Signaling Technology #3726, 1:200), rabbit anti-Rab5 (Cell Signaling Technology #3547, 1:400). Images were acquired using a Leica SP8 Lightning Confocal DMI6000 microscope. Images were analyzed using Imaris software.

Tissue preparation and immunohistochemistry

Postnatal (P7 and P21) mice were transcardially perfused with ice-cold PBS, followed by 4% PFA. Brains were removed and fixed in 4% PFA overnight upon collection. Brains were then cryopreserved in 30% sucrose for 48-72 hours, mounted in O.C.T. compound (Tissue-tek), and cryo-sectioned at 10-12 µm. For immunohistochemistry, frozen sections were dried at room temperature for 30 minutes and rehydrated in PBS with 0.1% Tween (PBSTw). Antigen retrieval was performed in 10mM citrate buffer, pH 6.0, for 20 minutes at 95° C. Sections were blocked with 10% normal goat serum in PBSTw for one hour at room temperature and incubated with primary antibodies in blocking solution overnight at 4° C, followed by incubation with fluorophore-conjugated secondary antibodies (1:200-500) and 1 µg/ml DAPI (Sigma-Aldrich) for one hour at room temperature. Sections were then mounted with glass coverslips using Aquamount (Fisher Scientific). The primary antibodies include: mouse anti-BrdU (DSHB #G3G4, 1:100), rat anti-BrdU (abcam #6326, 1:500), mouse anti-KCNB2 (NeuroMab #75-369, 1:100), mouse anti-PCNA (Santa Cruz Biotechnology #sc-56, 1:200), mouse anti-SOX2 (abcam #ab79351, 1:100), rabbit anti-SOX2 (abcam #ab97959, 1:200), rabbit anti-Caveolin-1 (Cell Signaling Technology #3267, 1:200), rabbit anti-DCX (abcam #ab18723, 1:200), rabbit anti-Ki67 (abcam #ab15580 1:200), rat anti-Ki67 (Ebioscience #14-5698-82, 1:200), rabbit anti-NeuN (abcam #ab104225, 1:200), rabbit anti-pEGFR (abcam #ab40815, 1:250), rabbit anti-pERK1/2 (Cell Signaling Technology #4370, 1:200),

rabbit anti-pERM (Cell Signaling Technology #3726, 1:200). Cell death was determined using TUNEL (Cat. # S7110, Sigma-Aldrich) according to the manufacturer's instructions. Images were acquired using a Leica SP8 confocal microscope or a Quorum spinning disc confocal microscope. Images were analyzed using Imaris software. Hematoxylin and eosin staining was performed on paraffin-embedded sections and imaged using a 3D Histech Pannoramic 250 Flash II Slide Scanner.

In vitro limiting dilution assay

Cells were plated in serial dilutions on non-adherent 96-well plates and in six biological replicates under stem cell conditions. Serial dilutions ranged from 2000 cells to 3 cells per well. After 7 days of plating, each well was scored for negative spheres. Data was plotted and tested for inequality in frequency between multiple groups and tested for adequacy of the single-hit model using Extreme Limiting Dilution Analysis (ELDA) software.

Atomic force microscopy

Force-displacement data were collected at room temperature using an AFM (Bioscope Catalyst, Santa Barbara, CA) mounted on an inverted microscope (Nikon Eclipse Ti2). Force-displacement-speed data were measured at the cell center. Measurement of cells in each petri dish was completed within 20 mins after being taken out of the incubator. The AFM probe with a spherical tip was used to measure the cell stiffness, using the Hertz model to calculate the cell stiffness value from the force-displacement data. The AFM probe with a needle shape tip was used to indent and penetrate the cell membrane, for measuring the cell membrane tension. The cell membrane tension results were calculated based on the force-displacement data before the membrane rupture was observed (larger than 100 pN) and using the mechanics model based on previous studies (Pietuch and Janshoff, 2013). The AFM probes used for cell stiffness measurement experiments were biosphere B100-CONT (Nanoandmore, USA), with a nominal spring constant of 0.2 N/m. The AFM probes used for cell membrane tension experiments were Focused-Ion-Beam modified probe MSNL-10 (Brucker, USA), with a nominal spring constant of 0.03 N/m (Wang et al., 2018). The spring constant of each probe was calibrated using thermal spectroscopy (Nanoscope 8.10). The loading speeds were set to be 10 μm/s to minimize the effects from the viscoelastic properties of the cell. Data analysis for quantifying cell stiffness and cell membrane tension was conducted in MATLAB. The code of data analysis for rejecting the non-rupture case is available for download at https://github.com/XianShawn/Nuclear_Mechanics.

Micropipette aspiration

The micropipette was fabricated from a glass capillary using a commercialized micropipette puller system (Model P-97, Sutter Instrument). The inner diameter of the micropipette tip is 2 μm. To make the tip horizontal under the microscope for clear aspiration observation, the tip was bent by 45° using a Microforge (Model MF-I, TPI Instruments). The pressure applied to the tip of the micropipette was controlled by a pneumatic microinjection pump (Digital Microinjector from Sutter Instrument). Before aspiration, a positive pressure was applied to the micropipette tip to balance the capillary force. During aspiration, the micropipette tip was gently brought into

contact with the cell surface and the pressure applied to the tip was reduced by a set amount. The entire aspiration process was recorded by a camera (scA1300-32gm, Basler) at 33 frames per second. The aspiration length and speed of the cell inside the micropipette was measured manually. The inner cell pressure was calculated using the standard linear solid model.

Electrophysiology

Cells were cultured on laminin-coated plastic coverslips for 48-72 hours. Coverslips were transferred to a recording chamber filled with bath solution. The bath solution consisted of (in mM) 118 NaCl, 3 KCl, 2.5 $CaCl_2$, 1.5 $MgCl_2$, 10 glucose, and 10 HEPES (PH adjusted to 7.4 with NaOH). Patch pipettes (borosilicate glass) for recording, with resistance of around 4 MΩ, were filled with intracellular solution consisting of 125 mM KCl, 11 mM EGTA, 1 mM $CaCl_2$, 1.5 mM $MgCl_2$, and 10 mM HEPES (PH adjusted to 7.2 with KOH). Whole-cell currents were recorded using an Axopatch 700B amplifier (Molecular Devices). All experiments were performed at room temperature. Pipette and whole cell capacitance were compensated. The voltage protocol consisted of 200 ms pulses from -80 mV to +80 mV (20 mV voltage steps). Data were acquired online, filtered at 4 kHz, digitized at 10 kHz, and analyzed offline using pClamp10 (Molecular Devices). Leak currents before voltage stimulations were subtracted off-line. I-V curves were generated by plotting peak current amplitude at different voltages. Data were quantified and graphed using GraphPad Prism.

Statistical analyses

No statistical methods were used to pre-determine sample sizes. The statistical analyses were performed after data collection without interim data analysis. No data points were excluded. Two-tailed Student's t-test was performed for comparison between two groups of samples. Two-Way ANOVA analyses were used to assess significance of multiple data points. The Kaplan–Meier estimator was used to generate survival curves using the R package {survival} (Therneau and Grambsch, 2000). Differences between survival curves were calculated using a log-rank test. All data were collected and processed randomly. All data are expressed as mean ± SEM. We considered a *P* value less than 0.05 to be statistically significant.

Key Resources Table

Reagent or Resource	Source	Identifier
4-Aminopyridine	TOCRIS	Cat# 0940
Accutase	Stem Cell Technologies	Cat# 07920
BrdU	Roche	Cat# 10280879001
Distilled water	Gibco	Cat# 15230147
Vismodegib (GDC-0449)	Selleck Chemicals	Cat# S1082
Human recombinant EGF	StemCell Technologies	Cat# 78006
Human TGF-α recombinant protein	Gibco	Cat# PHG0051

Laminin	Sigma-Aldrich	Cat# L2020
Methyl-β-cyclodextrin	Santa Cruz Biotechnology	Cat# sc-215379A
NeuroCult NS-A Basal Medium (Mouse)	StemCell Technologies	Cat# 05750
NSC668394	Sigma-Aldrich	Cat# 341216
Poly-L-ornithine	Sigma-Aldrich	Cat # P4957
Polyethylene Glycol 1500	Sigma-Aldrich	Cat # 10783641001
Recombinant Human Amphiregulin Protein	R&D Systems	Cat # 262-AR-100/CF
Apoptag Fluorescein In Situ Apoptosis Detection Kit	Millipore	Cat# 7110
4-Hydroxytamoxifen	Sigma	Cat# T5648
DMEM	Thermo Fisher	Cat# 11995073
FBS	Thermo Fisher	Cat# 12483020
Antibodies	**Source**	**Identifier**
Alexa Fluor 488 Phalloidin	Invitrogen	Cat# A12379; RRID: AB_2315147
chicken anti-GFP	Antibodies Incorporated	Cat# GFP-1020; RRID:AB_10000240
mouse anti-alpha-Tubulin	Sigma-Aldrich	Cat# T6199; RRID:AB_477583
mouse anti-BrdU (G3G4)	DSHB	Cat# G3G4; RRID:AB_2618097
mouse anti-Caveolin-1 (7C8)	Novus	Cat# NB100-615; RRID:AB_10003431
mouse anti-KCNB2 (N372B/1)	NeuroMab	Cat# 75-369; RRID: AB_2315870
mouse anti-PCNA (PC10)	Santa Cruz Biotechnology	Cat# sc-56; RRID:AB_628110
mouse anti-SOX2	abcam	Cat# ab79351; RRID:AB_10710406
rabbit anti-Caveolin-1 (D46G3)	Cell Signaling Technology	Cat# 3267; RRID:AB_2275453
rabbit anti-Clathrin Heavy Chain (D3C6)	Cell Signaling Technology	Cat# 4796; RRID:AB_10828486
rabbit anti-DCX	abcam	Cat# ab18723; RRID:AB_732011

rabbit anti-Ki67	abcam	Cat# ab15580; RRID:AB_443209
rabbit anti-NeuN	abcam	Cat# ab104225; RRID:AB_10711153
rabbit anti-pEGFR (Y1068)	Cell Signaling Technology	Cat# 3777; RRID:AB_2096270
rabbit anti-pEGFR (Y1068)	abcam	Cat# ab40815; RRID:AB_732110
rabbit anti-pERK1/2	Cell Signaling Technology	Cat# 4370; RRID:AB_2315112
rabbit anti-Phospho-Ezrin/Radixin/Moesin	Cell Signaling Technology	Cat# 3726; RRID:AB_10560513
rabbit anti-Rab5	Cell Signaling Technology	Cat# 3547; RRID:AB_2300649
rabbit anti-SOX2	abcam	Cat# ab97959; RRID:AB_2341193
rat anti-BrdU	abcam	Cat# ab6326; RRID:AB_305426
rat anti-Ki67 (SolA15)	Ebioscience	Cat# 14-5698-82; RRID:AB_10854564
anti-ERα	Santa Cruz Biotechnology	Cat # Sc-56833
DAPI	Sigma-Aldrich	Cat# D9564
Anti-hemagglutinin	Abcam	Cat # ab49969
Software and Algorithms	**Source**	**Identifier**
STAR (2.5.4b)	(Dobin et al., 2013)	https://github.com/alexdobin/STAR
R programming language (4.1.3)	(R Core Team, 2022)	https://www.R-project.org/
{DESeq2} (1.34.0)	(Love et al., 2014)	https://bioconductor.org/packages/release/bioc/html/DESeq2.html
{umap} (0.2.8.0)	(McInnes et al., 2020)	https://github.com/tkonopka/umap
{survival} (3.3-1)	(Therneau and Grambsch, 2000)	https://CRAN.R-project.org/package=survival
{Seurat} (4.1.0)	(Hao et al., 2021)	https://satijalab.org/seurat/
{Nebulosa} (1.4.0)	(Alquicira-Hernandez and Powell, 2021)	https://bioconductor.org/packages/release/bioc/html/Nebulosa.html

{harmony} (0.1.0)	(Korsunsky et al., 2019)	https://github.com/immunogenomics/harmony
Deposited Data	**Source**	**Identifier**
SHH MB scRNAseq normalized counts	(Hovestadt et al., 2019; Riemondy et al., 2021)	GEO: GSE119926 and GSE155446

RESOURCE AVAILABILITY

Lead Contact

For all additional information and request for resources and reagents should be directed to and will be fulfilled by the Lead Contacts, Dr. Xi Huang (xi.huang@sickkids.ca) and Dr. Michael Taylor (mdt.cns@gmail.com).

Materials Availability

All unique materials and reagents generated in this study can be obtained from the Lead Contact.

Figure 1

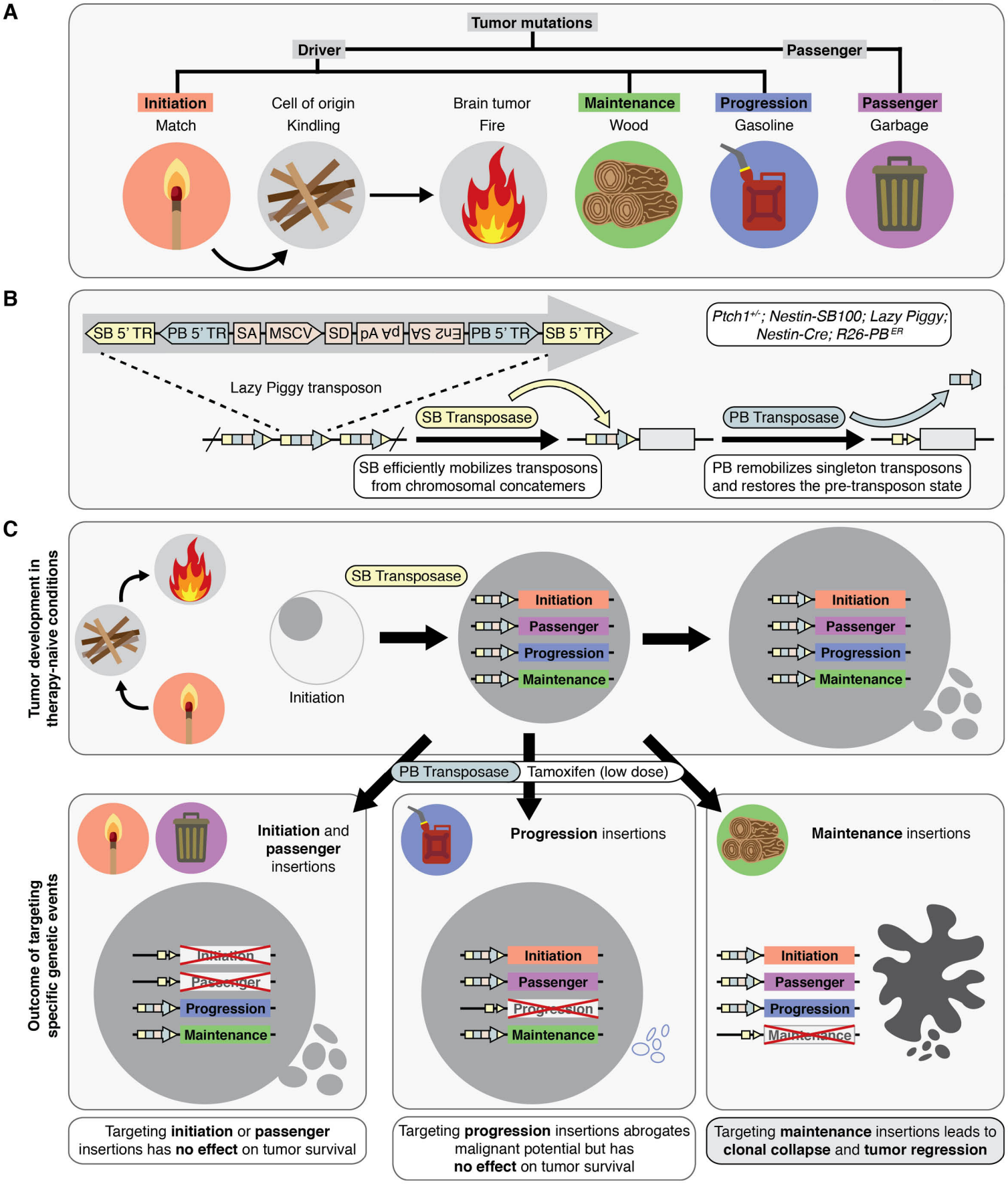
A
Tumor mutations
Driver
Passenger
Initiation
Match
Cell of origin
Kindling
Brain tumor
Fire
Maintenance
Wood
Progression
Gasoline
Passenger
Garbage
B
SB 5' TR
PB 5' TR
SA
MSCV
SD
pA
Ptch1+/-; Nestin-SB100; Lazy Piggy; Nestin-Cre; R26-PBER
Lazy Piggy transposon
SB Transposase
PB Transposase
SB efficiently mobilizes transposons from chromosomal concatemers
PB remobilizes singleton transposons and restores the pre-transposon state
C
Tumor development in therapy-naive conditions
SB Transposase
Initiation
Passenger
Progression
Maintenance
PB Transposase
Tamoxifen (low dose)
Outcome of targeting specific genetic events
Initiation and passenger insertions
Progression insertions
Maintenance insertions
Targeting initiation or passenger insertions has no effect on tumor survival
Targeting progression insertions abrogates malignant potential but has no effect on tumor survival
Targeting maintenance insertions leads to clonal collapse and tumor regression

Figure 2

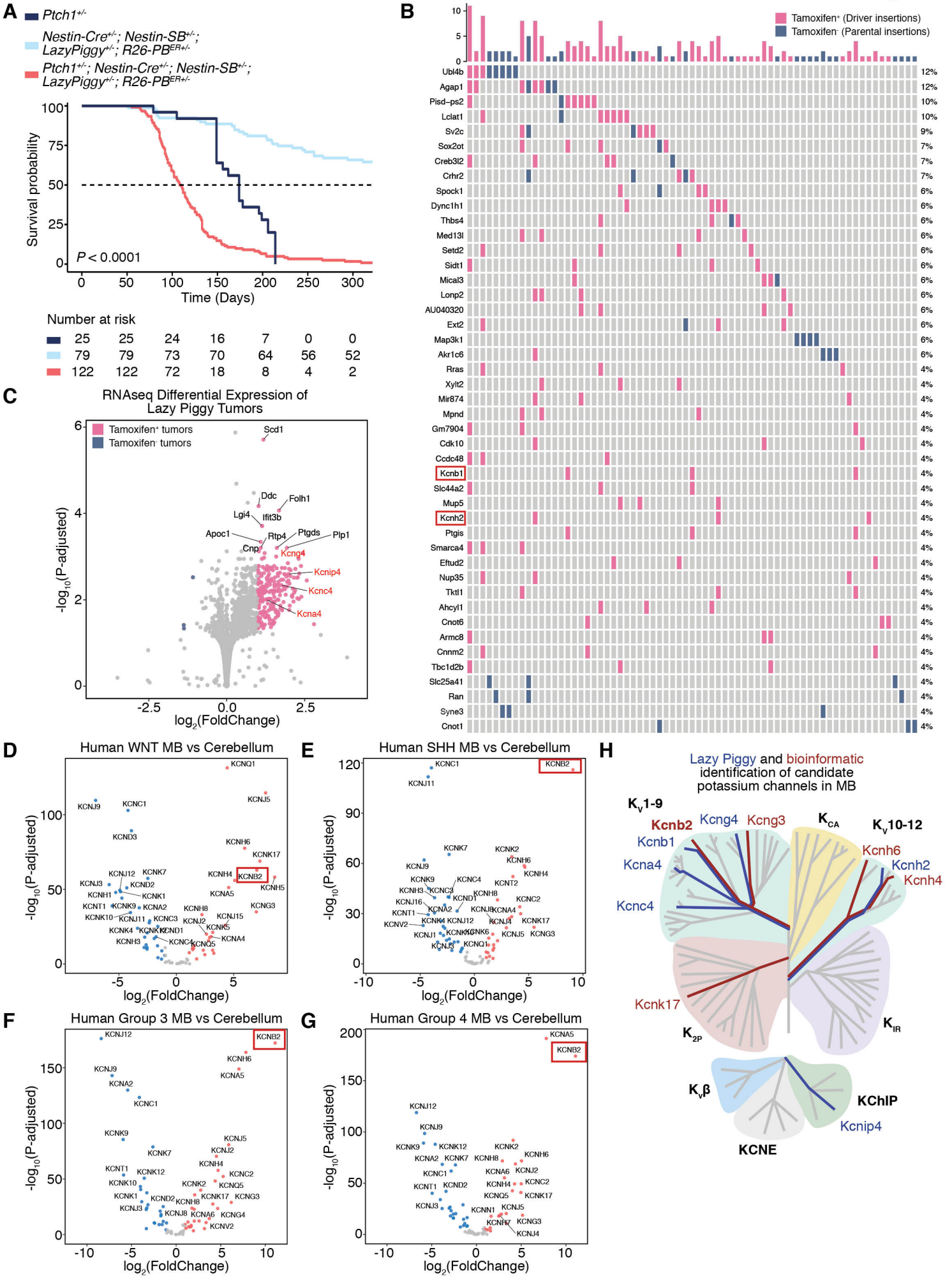
A
Ptch1+/-
Nestin-Cre+/-; Nestin-SB+/-; LazyPiggy+/-; R26-PBER+/-
Ptch1+/-; Nestin-Cre+/-; Nestin-SB+/-; LazyPiggy+/-; R26-PBER+/-
Survival probability
P < 0.0001
Time (Days)
Number at risk
25 25 24 16 7 0 0
79 79 73 70 64 56 52
122 122 72 18 8 4 2
B
Tamoxifen+ (Driver insertions)
Tamoxifen- (Parental insertions)
Ubl4b 12%
Agap1 12%
Pisd-ps2 10%
Lclat1 10%
Sv2c 9%
Sox2ot 7%
Creb3l2 7%
Crhr2 7%
Spock1 6%
Dync1h1 6%
Thbs4 6%
Med13l 6%
Setd2 6%
Sidt1 6%
Mical3 6%
Lonp2 6%
AU040320 6%
Ext2 6%
Map3k1 6%
Akr1c6 6%
Rras 4%
Xylt2 4%
Mir874 4%
Mpnd 4%
Gm7904 4%
Cdk10 4%
Ccdc48 4%
Kcnb1 4%
Slc44a2 4%
Mup5 4%
Kcnh2 4%
Ptgis 4%
Smarca4 4%
Eftud2 4%
Nup35 4%
Tktl1 4%
Ahcyl1 4%
Cnot6 4%
Armc8 4%
Cnnm2 4%
Tbc1d2b 4%
Slc25a41 4%
Ran 4%
Syne3 4%
Cnot1 4%
C
RNAseq Differential Expression of Lazy Piggy Tumors
Tamoxifen+ tumors
Tamoxifen- tumors
Scd1
Ddc
Folh1
Lgi4
Ifit3b
Apoc1
Rtp4
Ptgds
Plp1
Cnp
Kcng4
Kcnip4
Kcnc4
Kcna4
-log10(P-adjusted)
log2(FoldChange)
D
Human WNT MB vs Cerebellum
E
Human SHH MB vs Cerebellum
F
Human Group 3 MB vs Cerebellum
G
Human Group 4 MB vs Cerebellum
H
Lazy Piggy and bioinformatic identification of candidate potassium channels in MB
Kv1-9
Kcnb2
Kcng4
Kcng3
KCA
Kv10-12
Kcnb1
Kcna4
Kcnh6
Kcnh2
Kcnh4
Kcnc4
Kcnk17
K2P
KIR
Kvβ
KChIP
Kcnip4
KCNE

Figure 3

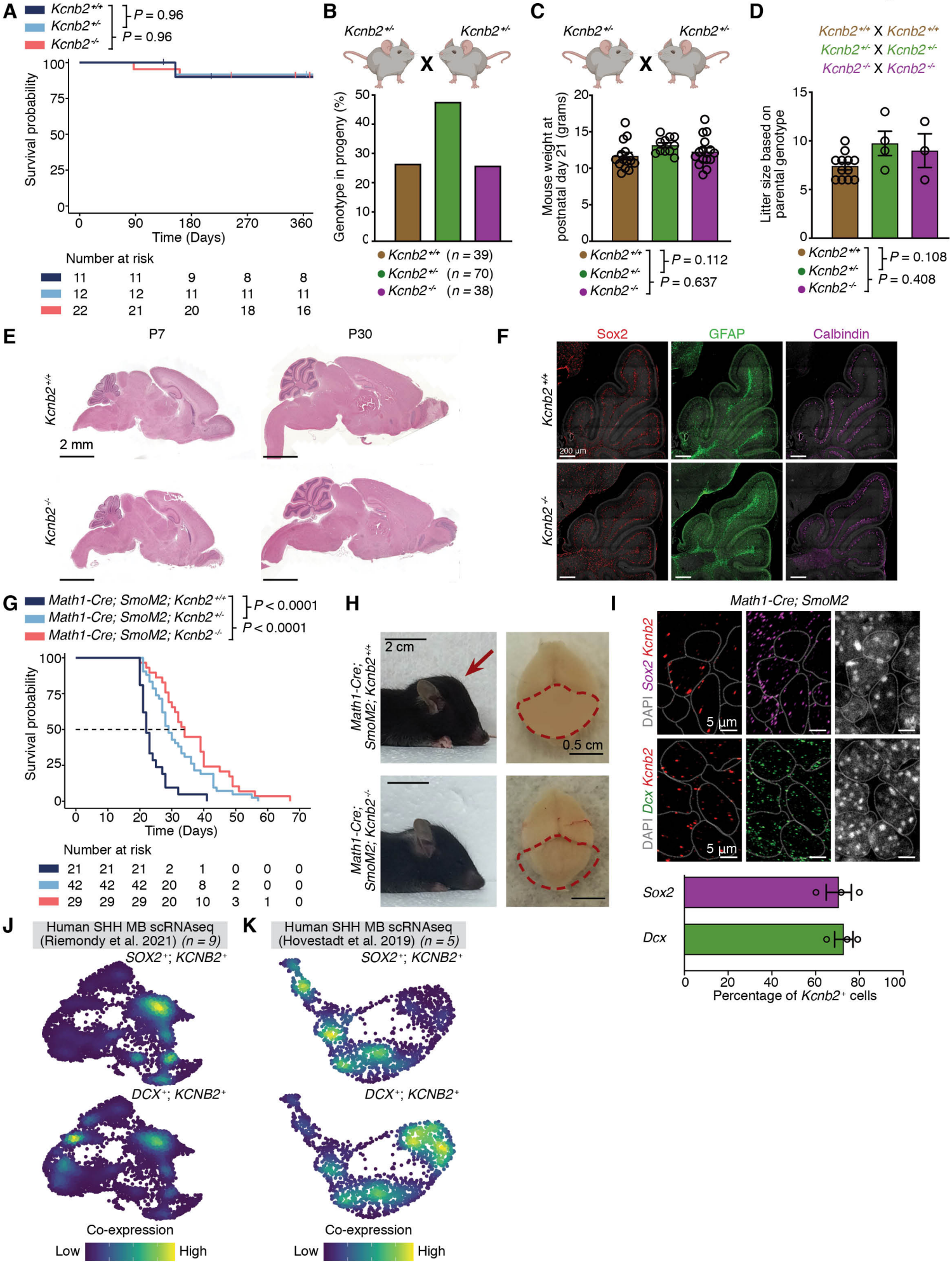
A
Kcnb2+/+
Kcnb2+/-
Kcnb2-/-
P = 0.96
P = 0.96
Survival probability
Time (Days)
Number at risk
11 11 9 8 8
12 12 11 11 11
22 21 20 18 16
B
Kcnb2+/-
Kcnb2+/-
Genotype in progeny (%)
Kcnb2+/+ (n = 39)
Kcnb2+/- (n = 70)
Kcnb2-/- (n = 38)
C
Kcnb2+/-
Kcnb2+/-
Mouse weight at postnatal day 21 (grams)
P = 0.112
P = 0.637
D
Kcnb2+/+ X Kcnb2+/+
Kcnb2+/- X Kcnb2+/-
Kcnb2-/- X Kcnb2-/-
Litter size based on parental genotype
P = 0.108
P = 0.408
E
P7
P30
Kcnb2+/+
Kcnb2-/-
2 mm
F
Sox2
GFAP
Calbindin
200 µm
G
Math1-Cre; SmoM2; Kcnb2+/+
Math1-Cre; SmoM2; Kcnb2+/-
Math1-Cre; SmoM2; Kcnb2-/-
P < 0.0001
P < 0.0001
Survival probability
Time (Days)
Number at risk
21 21 21 2 1 0 0 0
42 42 42 20 8 2 0 0
29 29 29 20 10 3 1 0
H
Math1-Cre; SmoM2; Kcnb2+/+
Math1-Cre; SmoM2; Kcnb2-/-
2 cm
0.5 cm
I
Math1-Cre; SmoM2
DAPI Sox2 Kcnb2
DAPI Dcx Kcnb2
5 µm
Sox2
Dcx
Percentage of Kcnb2+ cells
J
Human SHH MB scRNAseq (Riemondy et al. 2021) (n = 9)
SOX2+; KCNB2+
DCX+; KCNB2+
Co-expression
Low
High
K
Human SHH MB scRNAseq (Hovestadt et al. 2019) (n = 5)
SOX2+; KCNB2+
DCX+; KCNB2+
Co-expression
Low
High

Figure 4

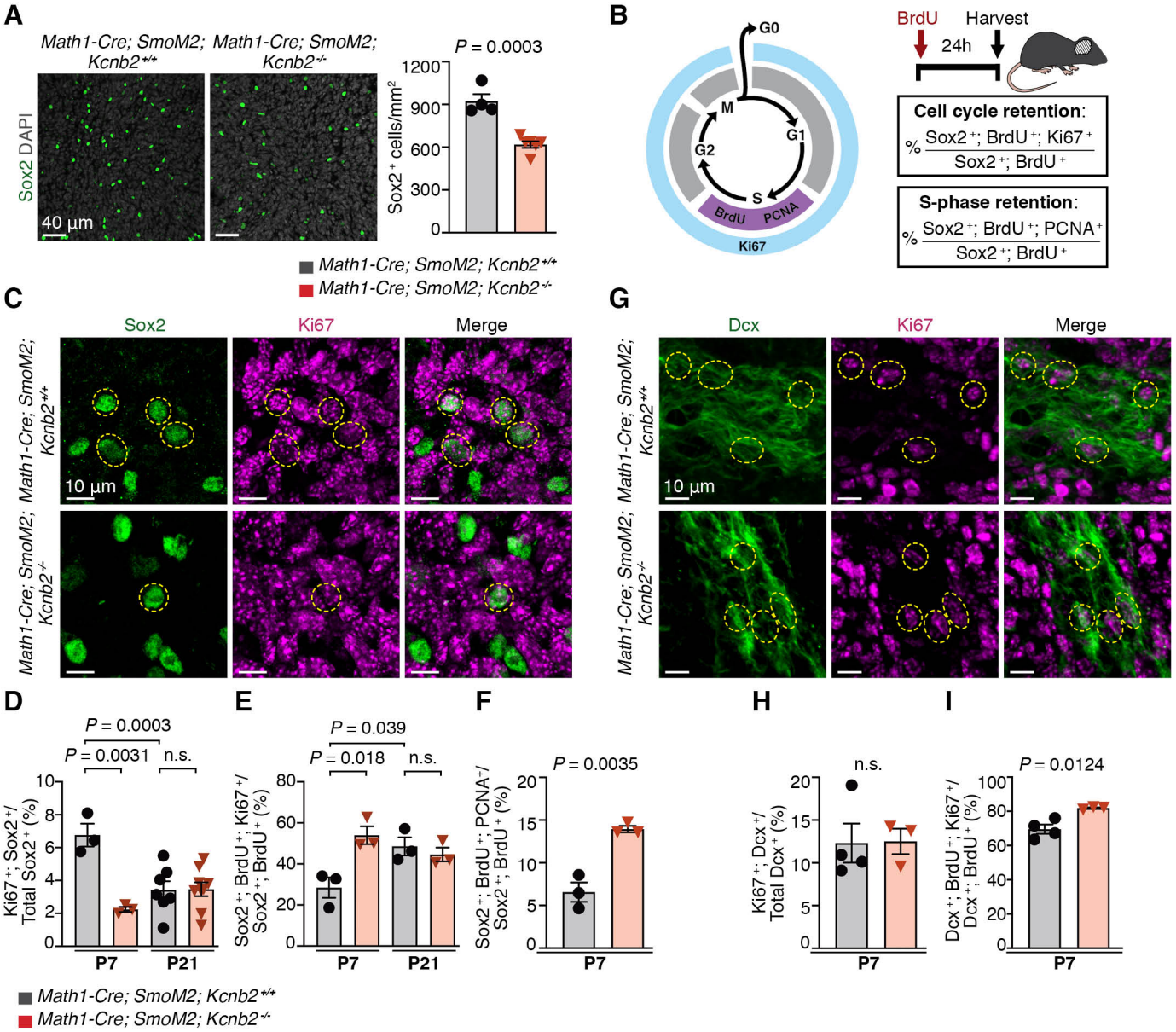
A
Math1-Cre; SmoMz; Kcnb2+/+
Math1-Cre; SmoMz; Kcnb2-/-
Sox2 DAPI
40 µm
P = 0.0003
Sox2+ cells/mm2
1200
900
600
300
0
Math1-Cre; SmoMz; Kcnb2+/+
Math1-Cre; SmoMz; Kcnb2-/-
B
G0
M
G1
G2
S
BrdU
PCNA
Ki67
BrdU
Harvest
24h
Cell cycle retention:
% Sox2+; BrdU+; Ki67+ / Sox2+; BrdU+
S-phase retention:
% Sox2+; BrdU+; PCNA+ / Sox2+; BrdU+
C
Sox2
Ki67
Merge
Math1-Cre; SmoMz; Kcnb2+/+
Math1-Cre; SmoMz; Kcnb2-/-
10 µm
G
Dcx
Ki67
Merge
Math1-Cre; SmoMz; Kcnb2+/+
Math1-Cre; SmoMz; Kcnb2-/-
10 µm
D
P = 0.0003
P = 0.0031
n.s.
Ki67+; Sox2+/ Total Sox2+ (%)
P7
P21
E
P = 0.039
P = 0.018
n.s.
Sox2+; BrdU+; Ki67+/ Sox2+; BrdU+ (%)
P7
P21
F
P = 0.0035
Sox2+; BrdU+; PCNA+/ Sox2+; BrdU+ (%)
P7
H
n.s.
Ki67+; Dcx+/ Total Dcx+ (%)
P7
I
P = 0.0124
Dcx+; BrdU+; Ki67+/ Dcx+; BrdU+ (%)
P7
Math1-Cre; SmoMz; Kcnb2+/+
Math1-Cre; SmoMz; Kcnb2-/-

Figure 5

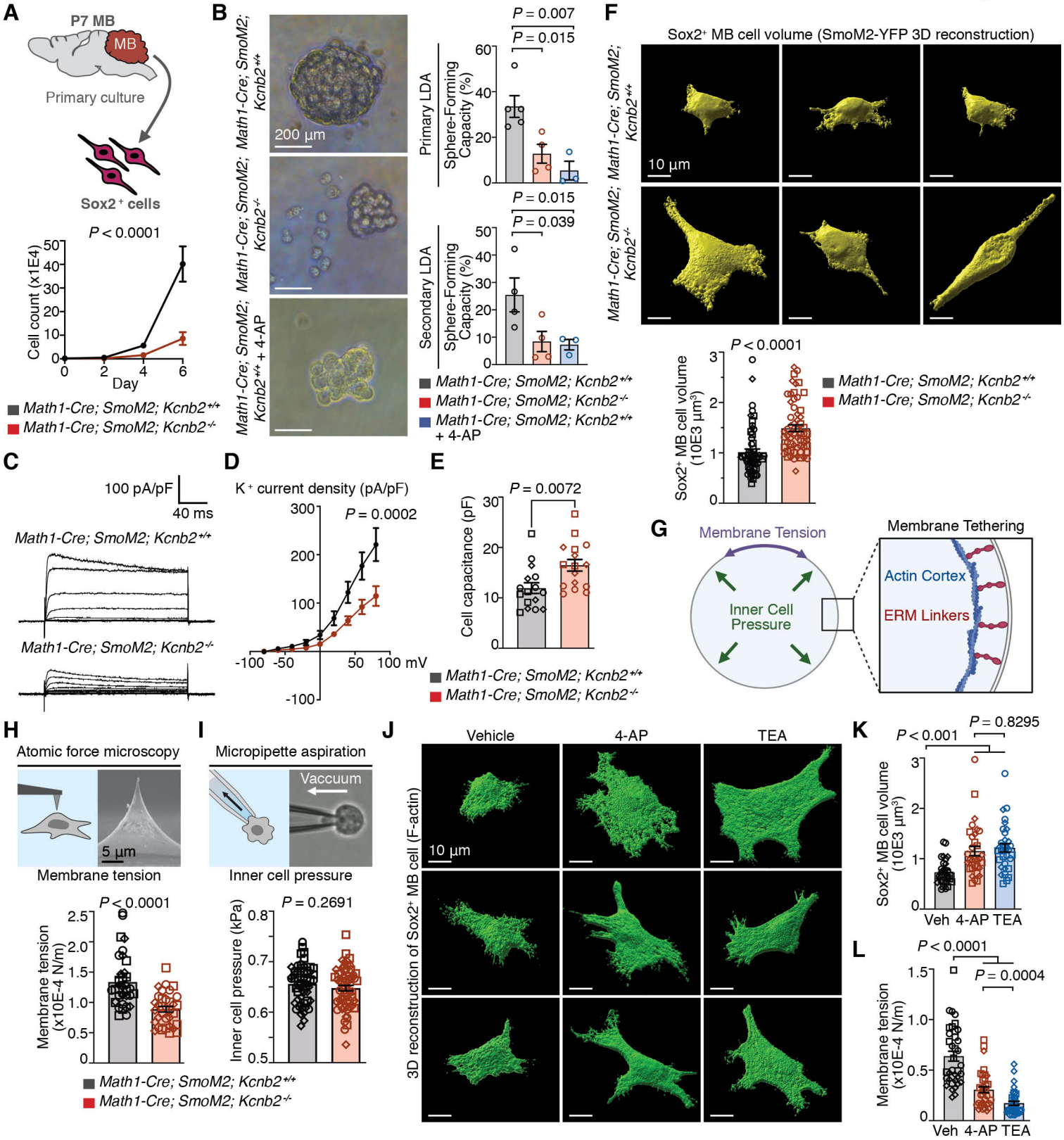
A
P7 MB
MB
Primary culture
Sox2⁺ cells
P < 0.0001
Cell count (x1E4)
Day
Math1-Cre; SmoM2; Kcnb2+/+
Math1-Cre; SmoM2; Kcnb2-/-
B
Math1-Cre; SmoM2; Kcnb2+/+
Math1-Cre; SmoM2; Kcnb2-/-
Math1-Cre; SmoM2; Kcnb2+/+ + 4-AP
200 µm
P = 0.007
P = 0.015
Primary LDA
Sphere-Forming Capacity (%)
P = 0.015
P = 0.039
Secondary LDA
Math1-Cre; SmoM2; Kcnb2+/+
Math1-Cre; SmoM2; Kcnb2-/-
Math1-Cre; SmoM2; Kcnb2+/+ + 4-AP
F
Sox2⁺ MB cell volume (SmoM2-YFP 3D reconstruction)
10 µm
P < 0.0001
Sox2⁺ MB cell volume (10E3 µm³)
Math1-Cre; SmoM2; Kcnb2+/+
Math1-Cre; SmoM2; Kcnb2-/-
C
100 pA/pF
40 ms
Math1-Cre; SmoM2; Kcnb2+/+
Math1-Cre; SmoM2; Kcnb2-/-
D
K⁺ current density (pA/pF)
P = 0.0002
mV
E
P = 0.0072
Cell capacitance (pF)
Math1-Cre; SmoM2; Kcnb2+/+
Math1-Cre; SmoM2; Kcnb2-/-
G
Membrane Tension
Inner Cell Pressure
Membrane Tethering
Actin Cortex
ERM Linkers
H
Atomic force microscopy
5 µm
Membrane tension
P < 0.0001
Membrane tension (x10E-4 N/m)
I
Micropipette aspiration
Vaccuum
Inner cell pressure
P = 0.2691
Inner cell pressure (kPa)
Math1-Cre; SmoM2; Kcnb2+/+
Math1-Cre; SmoM2; Kcnb2-/-
J
Vehicle
4-AP
TEA
3D reconstruction of Sox2⁺ MB cell (F-actin)
10 µm
K
P < 0.001
P = 0.8295
Sox2⁺ MB cell volume (10E3 µm³)
Veh
4-AP
TEA
L
P < 0.0001
P = 0.0004
Membrane tension (x10E-4 N/m)
Veh
4-AP
TEA

Figure 6

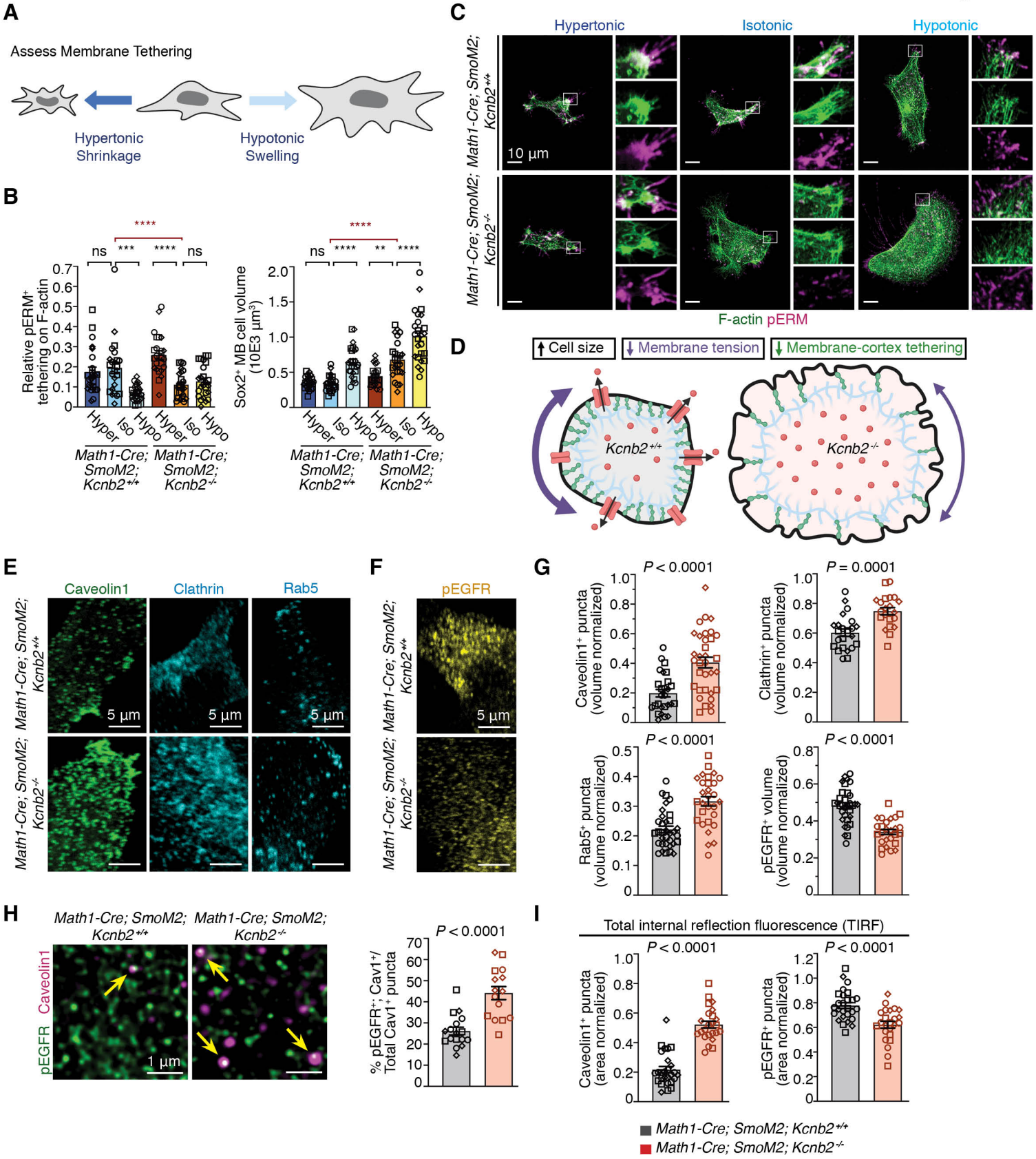
A
Assess Membrane Tethering
Hypertonic Shrinkage
Hypotonic Swelling
B
Relative pERM+ tethering on F-actin
Sox2+ MB cell volume (10E3 µm3)
Hyper
Iso
Hypo
Math1-Cre; SmoM2; Kcnb2+/+
Math1-Cre; SmoM2; Kcnb2-/-
C
Hypertonic
Isotonic
Hypotonic
10 µm
F-actin pERM
D
Cell size
Membrane tension
Membrane-cortex tethering
Kcnb2+/+
Kcnb2-/-
E
Caveolin1
Clathrin
Rab5
5 µm
F
pEGFR
G
Caveolin1+ puncta (volume normalized)
Clathrin+ puncta (volume normalized)
Rab5+ puncta (volume normalized)
pEGFR+ volume (volume normalized)
P < 0.0001
P = 0.0001
H
Caveolin1
pEGFR
1 µm
% pEGFR+; Cav1+/ Total Cav1+ puncta
I
Total internal reflection fluorescence (TIRF)
Caveolin1+ puncta (area normalized)
pEGFR+ puncta (area normalized)
Math1-Cre; SmoM2; Kcnb2+/+
Math1-Cre; SmoM2; Kcnb2-/-

Figure 7

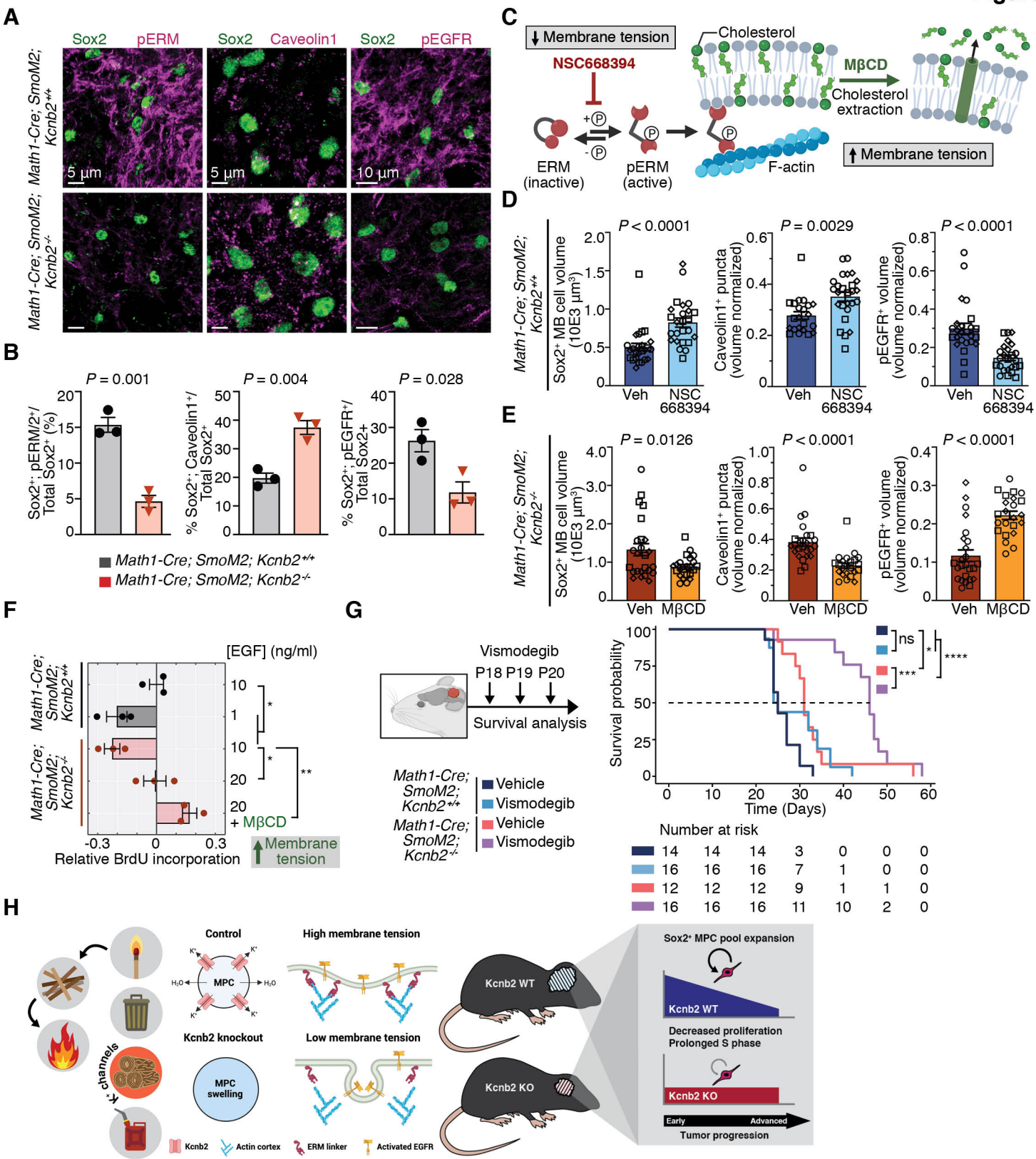
A
Sox2
pERM
Caveolin1
pEGFR
Math1-Cre; SmoM2; Kcnb2+/+
Math1-Cre; SmoM2; Kcnb2-/-
5 µm
10 µm
B
P = 0.001
P = 0.004
P = 0.028
Sox2+; pERM/2+/ Total Sox2+ (%)
% Sox2+; Caveolin1+/ Total Sox2+
% Sox2+; pEGFR+/ Total Sox2+
Math1-Cre; SmoM2; Kcnb2+/+
Math1-Cre; SmoM2; Kcnb2-/-
C
Membrane tension
NSC668394
ERM (inactive)
pERM (active)
Cholesterol
MβCD
Cholesterol extraction
F-actin
Membrane tension
D
P < 0.0001
P = 0.0029
P < 0.0001
Sox2+ MB cell volume (10E3 µm3)
Caveolin1+ puncta (volume normalized)
pEGFR+ volume (volume normalized)
Veh
NSC 668394
E
P = 0.0126
P < 0.0001
P < 0.0001
Sox2+ MB cell volume (10E3 µm3)
Caveolin1+ puncta (volume normalized)
pEGFR+ volume (volume normalized)
Veh
MβCD
F
[EGF] (ng/ml)
Math1-Cre; SmoM2; Kcnb2+/+
Math1-Cre; SmoM2; Kcnb2-/-
+ MβCD
Relative BrdU incorporation
Membrane tension
G
Vismodegib
P18 P19 P20
Survival analysis
Math1-Cre; SmoM2; Kcnb2+/+
Vehicle
Vismodegib
Math1-Cre; SmoM2; Kcnb2-/-
Vehicle
Vismodegib
Survival probability
Time (Days)
ns
Number at risk
14 14 14 3 0 0 0
16 16 16 7 1 0 0
12 12 12 9 1 1 0
16 16 16 11 10 2 0
H
Control
High membrane tension
MPC
Kcnb2 knockout
Low membrane tension
MPC swelling
K+ channels
Kcnb2
Actin cortex
ERM linker
Activated EGFR
Kcnb2 WT
Kcnb2 KO
Sox2+ MPC pool expansion
Decreased proliferation
Prolonged S phase
Early
Advanced
Tumor progression

Supplemental Figure 1

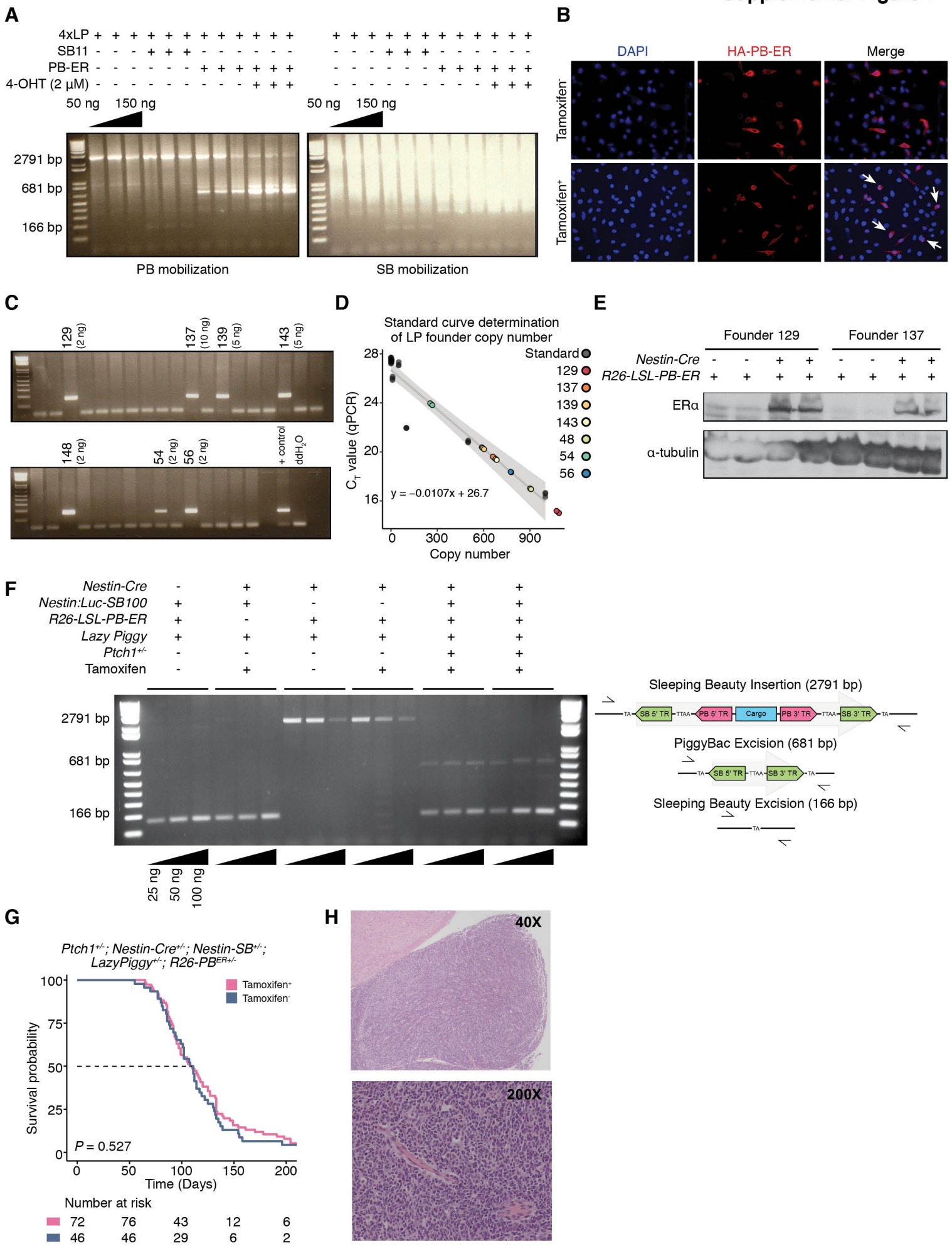

Supplemental Figure 2

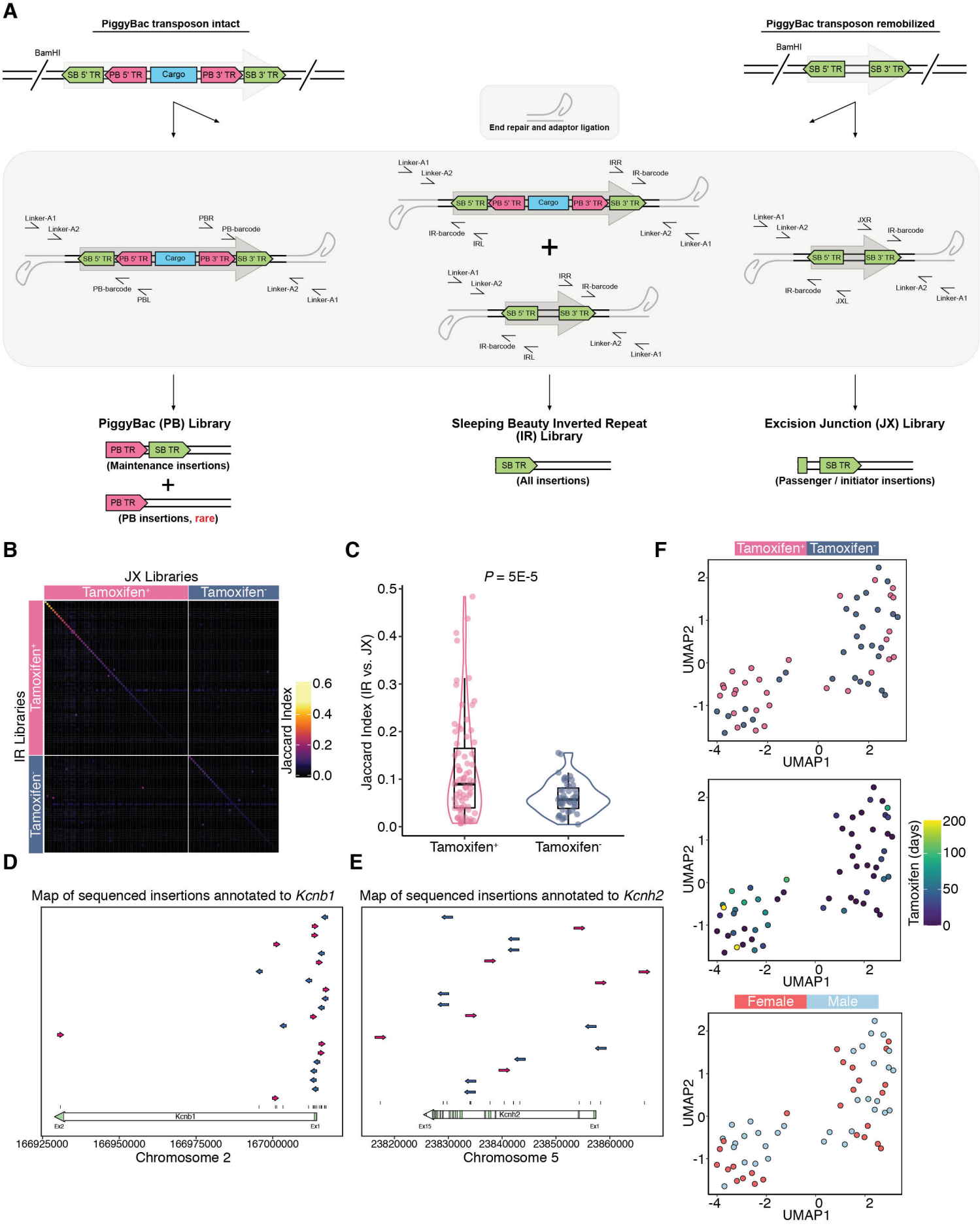

Supplemental Figure 3

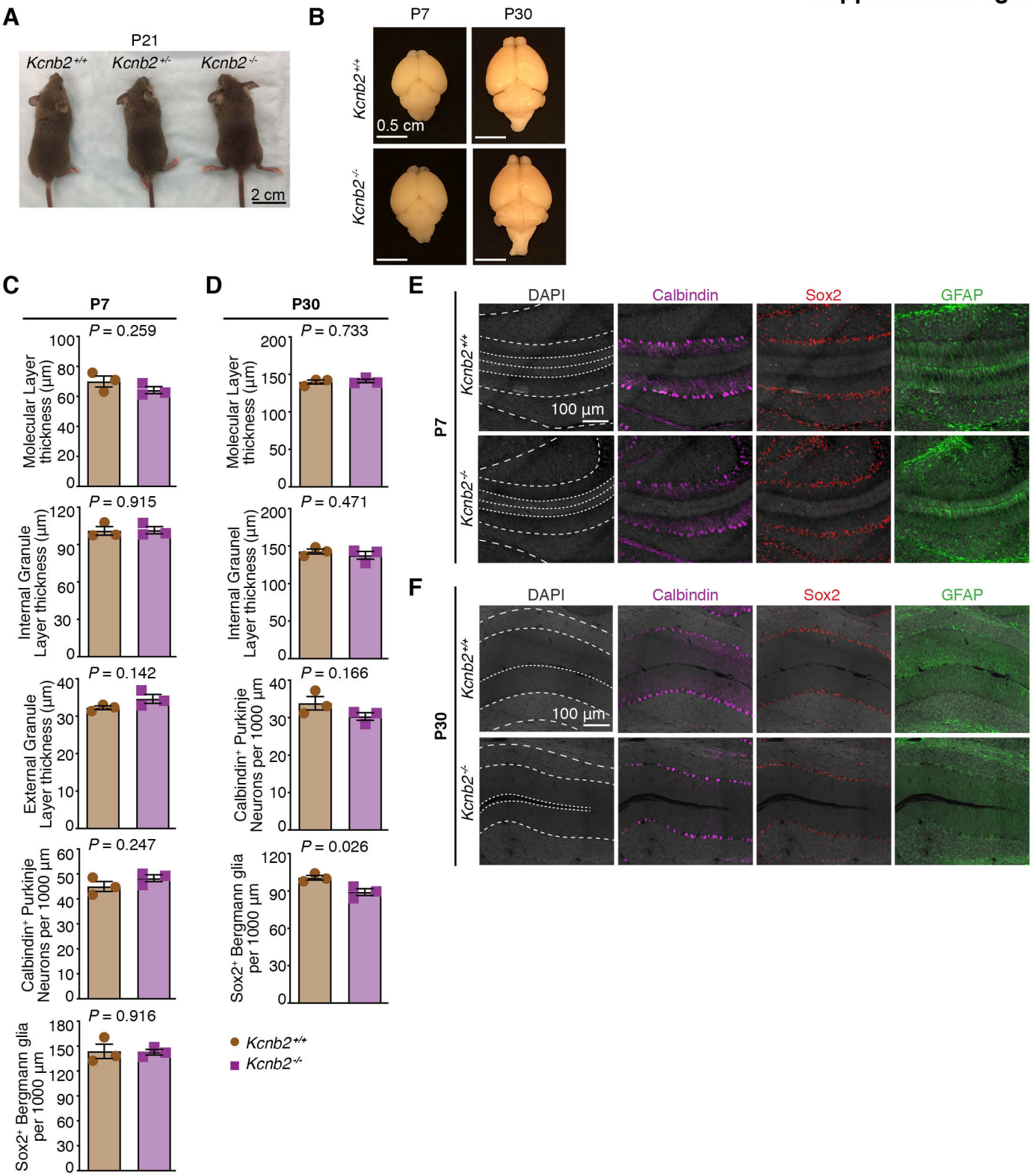

Supplemental Figure 4

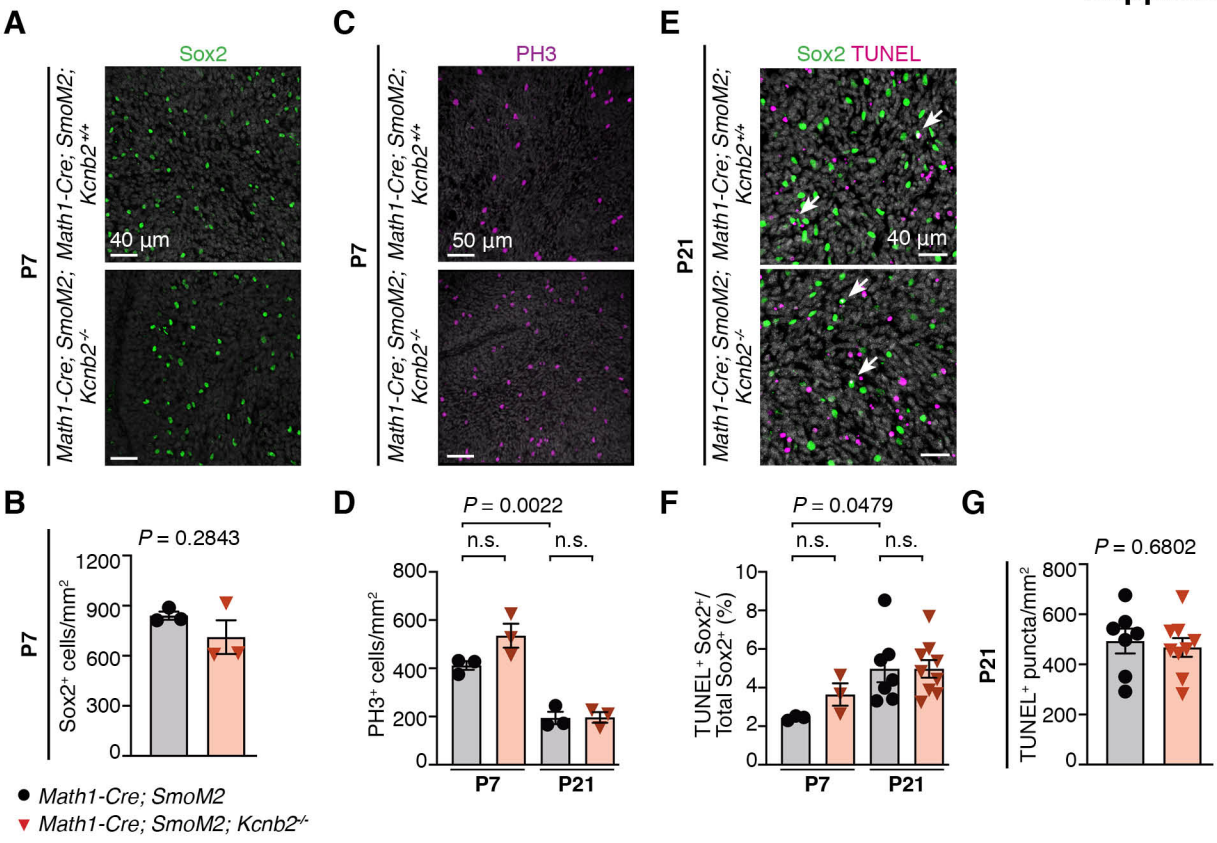

Supplemental Figure 5

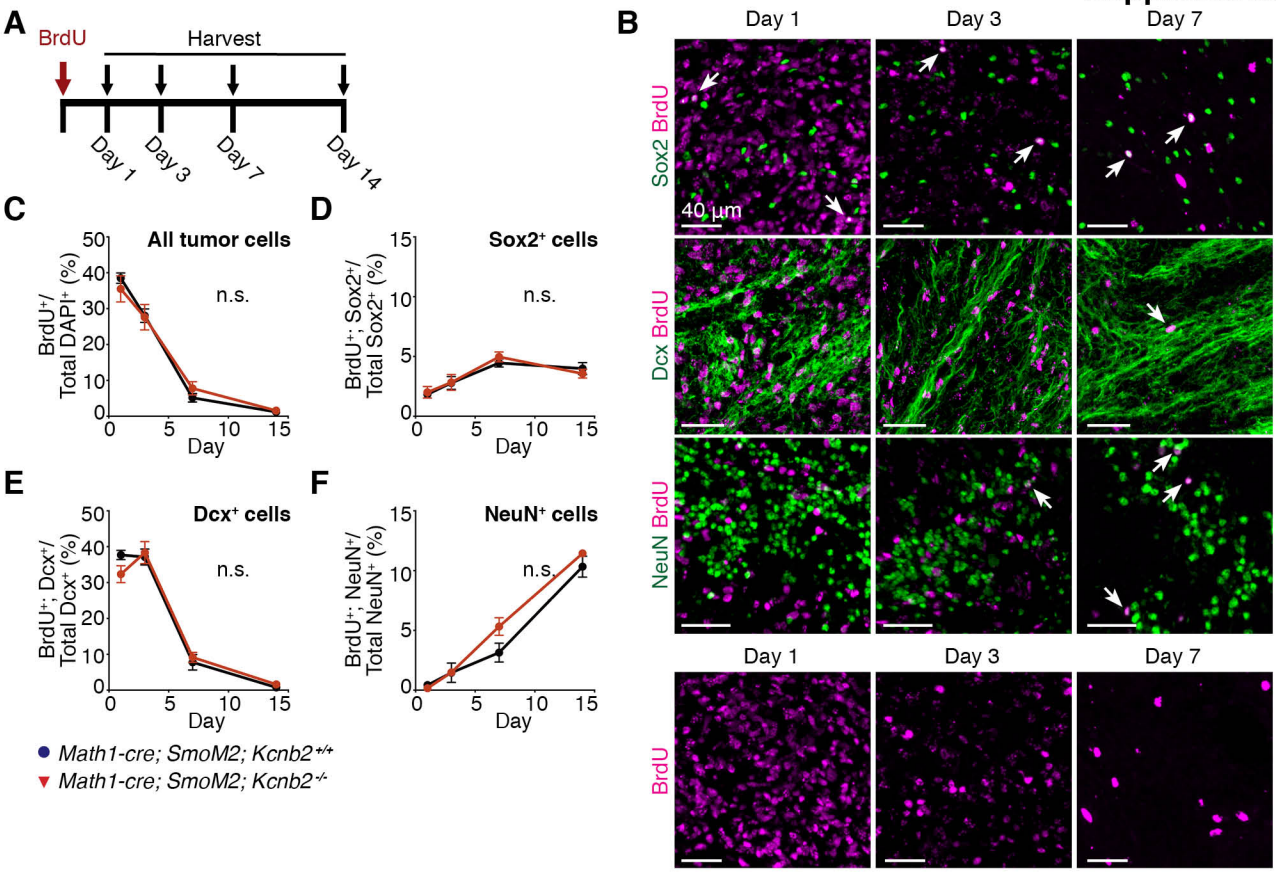
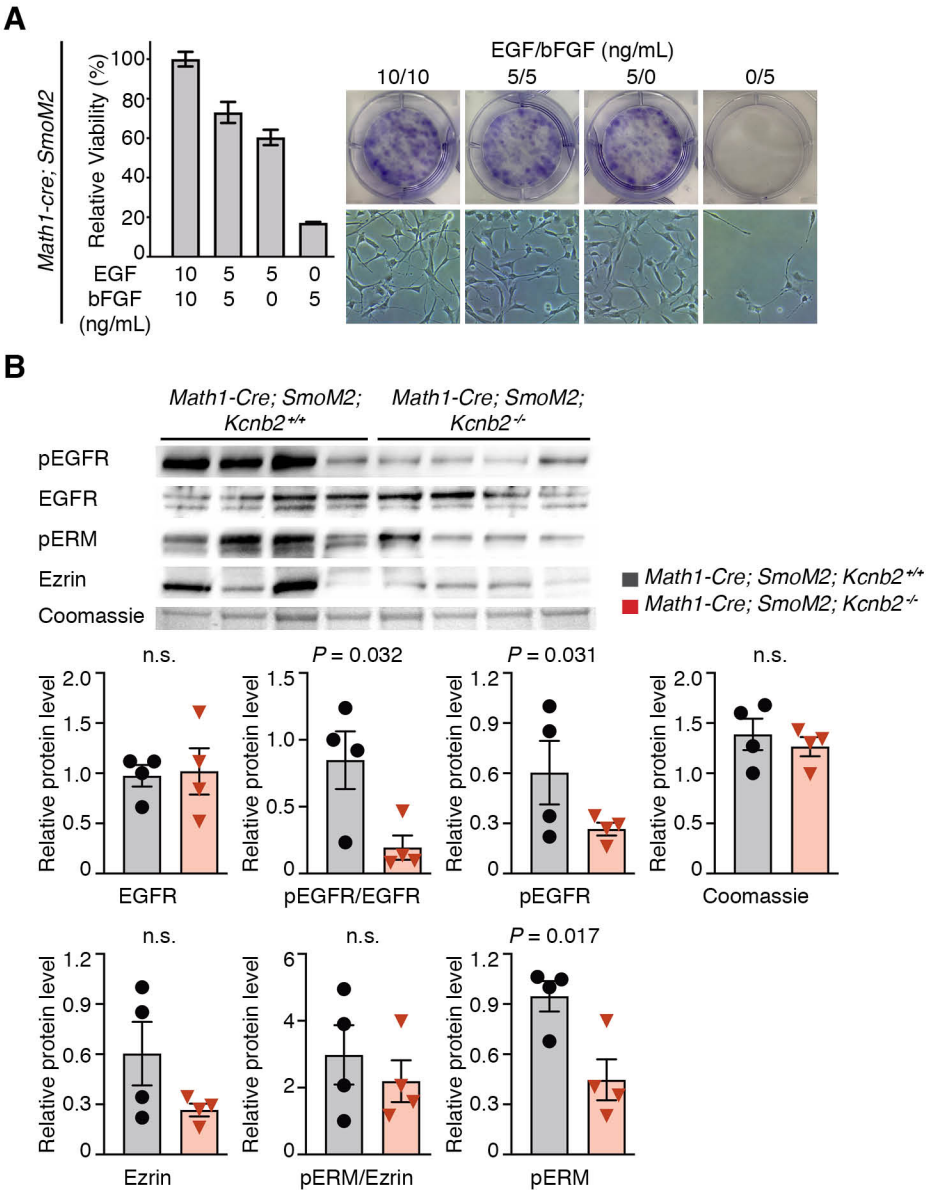
Supplemental Figure 6